PROCEEDINGS A

royalsocietypublishing.org/journal/rspa

Research

Cite this article: Schimming CD, Viñals J. 2023 Kinematics and dynamics of disclination lines in three-dimensional nematics. *Proc. R. Soc. A* **479**: 20230042.
https://doi.org/10.1098/rspa.2023.0042

Received: 31 January 2023
Accepted: 28 April 2023

Subject Areas:
materials science

Keywords:
topological defects, disclinations, liquid crystals, nematic phases

Author for correspondence:
Cody D. Schimming
e-mail: cschim@lanl.gov

Electronic supplementary material is available online at https://doi.org/10.6084/m9.figshare.c.6644164.

THE ROYAL SOCIETY PUBLISHING

Downloaded from https://royalsocietypublishing.org/ on 06 November 2023

Kinematics and dynamics of disclination lines in three-dimensional nematics

Cody D. Schimming[1] and Jorge Viñals[2]

[1]Theoretical Division and Center for Nonlinear Studies (CNLS), Los Alamos National Laboratory, Los Alamos, NM 87545, USA
[2]School of Physics and Astronomy, University of Minnesota, Minneapolis, MN 55455, USA

CDS, 0000-0003-2143-6738

An exact kinematic law for the motion of disclination lines in nematic liquid crystals as a function of the tensor order parameter $\mathbf{Q}$ is derived. Unlike other order parameter fields that become singular at their respective defect cores, the tensor order parameter remains regular. Following earlier experimental and theoretical work, the disclination core is defined to be the line where the uniaxial and biaxial order parameters are equal, or equivalently, where the two largest eigenvalues of $\mathbf{Q}$ cross. This allows an exact expression relating the velocity of the line to spatial and temporal derivatives of $\mathbf{Q}$ on the line, to be specified by a dynamical model for the evolution of the nematic. By introducing a linear core approximation for $\mathbf{Q}$, analytical results are given for several prototypical configurations, including line interactions and motion, loop annihilation, and the response to external fields and shear flows. Behaviour that follows from topological constraints or defect geometry is highlighted. The analytic results are shown to be in agreement with three-dimensional numerical calculations based on a singular Maier–Saupe free energy that allows for anisotropic elasticity.

1. Introduction

Topological defects play an integral role in the response and non-equilibrium evolution of many physical systems: in type-II superconductors, for example, vortices allow magnetic field lines to penetrate the material and dissipate [1,2]; in solids, dislocations mediate plastic deformation and melting [3–6]; in developing biological tissue, defects indicate sites of further morphogenesis

© 2023 The Author(s) Published by the Royal Society. All rights reserved.

Downloaded from https://royalsocietypublishing.org/ on 06 November 2023

and curvature generation [7–9]; and in nematic liquid crystals, disclinations promote aggregation of colloidal particles and generate fluid velocity in active materials [10–14]. Therefore, significant efforts are under way to further elucidate the general principles behind their dynamics [2,15–27]. A common theoretical strategy is to treat defects as effective 'particles'. This is made possible by topological constraints: defects cannot spontaneously disappear or nucleate, but must instead pairwise annihilate or unbind (similar to particles and antiparticles). Additionally, topological defect charges can be quantized, that is, related to the non-trivial homotopy group of the physical system [17,28]. Thus, in those cases in which the response or the temporal evolution of a system are determined by the nature and distribution of defects (with the overall dynamics slaved to such a distribution), one needs only focus on laws of motion for the effective 'particles' (or 'strings' or 'membranes' for higher-dimensional defects).

Our focus here is on topological defects in nematic phases (disclinations). In a nematic, the order parameter is a symmetric, traceless tensor, $\mathbf{Q}$, which captures both rotational and apolar symmetries. Nematics are well known for their anisotropic optical and hydrodynamic properties [29–31]; however, there has been increasing interest in the role of disclinations in both passive and active nematics. In the former, disclinations mediate colloidal aggregation and can be patterned to engineer transport throughout the material [10,11,32–36]. In the latter, disclinations form spontaneously, and generate flows depending on their topological or geometric character [13,14,24,37].

In this work, a particle-field transformation is introduced to describe disclination line motion in nematic phases. Such a transformation relating the location of the line to the field equations governing the evolution of the nematic tensor order parameter allows for an exact kinematic law of motion for the disclination, independent of the microscopic model governing the evolution of nematic order. The type of particle-field transformation that we introduce has been successfully used to analyse and track vortex motion in superfluids [38], the motion of point defects in n-vector models [39–41], and, more recently, the motion of dislocations in solids in both two [22,42] and three dimensions [43]. The method has also been used to describe disclination motion in nematic active matter, albeit in two spatial dimensions [44].

Despite recent interest in the motion of disclinations in nematic phases, there are still many open questions regarding their structure and motion, particularly in three dimensions. While the topological structure is deceptively simple (the first fundamental group in three dimensions is $\mathbb{Z}_2$ instead of $\mathbb{Z}$ in two dimensions), the geometric character of the defect is completely different. Nematic disclinations in two dimensions are point defects, whereas line disclinations in three dimensions are spatially extended, and generally described by two independent vectors: the tangent vector to the disclination $\hat{\mathbf{T}}$, and the rotation vector describing the nematic distortion near the defect $\hat{\boldsymbol{\Omega}}$ [29,45]. Further, and unlike all the applications of particle-field transformations mentioned above, the tensor order parameter is regular at the disclination core [46–48]. Hence the core is not defined by the well-studied director phase singularity, rather by a crossing of eigenvalues of the tensor order parameter.

We first introduce the particle-field transformation to a nematic phase in three dimensions described by a tensor order parameter $\mathbf{Q}$. Even though the order parameter does not go to zero at defect locations, a quantity defined on a subspace of the order parameter space does, a fact that is used to locate disclination cores. The transformation leads to a kinematic law which is then used to obtain analytic predictions of disclination motion using suitable approximations of the order parameter in the vicinity of the core. Disclination velocity is seen to be determined by gradients of the tensor order parameter at the core, a fact that significantly simplifies consideration of a number of prototypical configurations involving lines, loops, and their interactions. Within a linear core approximation for the order parameter, we obtain analytic results for the evolution of both optimally oriented and twisted defect configurations, including elastic anisotropy, find transverse defect mobilities of topological origin, study disclination line interaction and recombination, loop shrinkage, and show that external fields or imposed shear flows can spatially separate (sort) lines and loops according to their topological charge distribution. Transverse

Downloaded from https://royalsocietypublishing.org/ on 06 November 2023

mobilities and defect sorting are important for the many applications that rely on defect control and defect engineering which are currently under development in soft, active and biological matter. Importantly, the motion that follows derives not only from the forces among disclination segments, but also incorporates the necessary topological constraints explicit in the kinematic law. Although our main focus is on nematic liquid crystals, the techniques described should apply to a range of complex systems in which topological defects are allowed.

The rest of the paper is organized as follows: in §2, we briefly review the structure of the disclination core in three-dimensional nematics. In §3, we use the fact that the eigenvalues of the order parameter $\mathbf{Q}$ cross at the disclination core to derive a kinematic velocity equation in terms of the order parameter. In §4, we describe an analytical approximation of $\mathbf{Q}$ near the core (the 'linear core approximation'), and show how this approximation may be used to obtain the velocity of a disclination in the presence of an imposed rotation of the director (this is the analogue of the Peach–Koehler force in elasticity theory). In §5, we present analytical predictions for the motion of disclinations in both two- and three-dimensional configurations involving disclination annihilation and exposure to external fields and flows. Throughout we supplement our analysis with numerical calculations in two and three dimensions, and find excellent agreement between the two despite the complicated nonlinearities present in the computational model. Finally, in §6 we discuss our results and their implications for nematics and other systems in which disclinations are pervasive. We also discuss potential further work in understanding disclination dynamics.

2. Disclination core structure

Consider an ensemble of nematogens, each described by a unit vector $\hat{\boldsymbol{\xi}}$ giving its molecular orientation. Let $p(\hat{\boldsymbol{\xi}})$ be the equilibrium probability density of orientations at constant temperature, defined on the unit sphere $\mathcal{S}^2$. The tensor order parameter is defined as

$$\mathbf{Q} = \int_{\mathcal{S}^2} \left(\hat{\boldsymbol{\xi}} \otimes \hat{\boldsymbol{\xi}} - \frac{1}{3}\mathbf{I} \right) p(\hat{\boldsymbol{\xi}}) \, \mathrm{d}\Sigma(\hat{\boldsymbol{\xi}}), \tag{2.1}$$

where $\mathbf{Q}$ can be uniform or a field if distorted configurations at the mesoscale are considered. With this definition, the tensor $\mathbf{Q}$ is symmetric and traceless, and can be represented as $\mathbf{Q} = S[\hat{\mathbf{n}} \otimes \hat{\mathbf{n}} - (1/3)\mathbf{I}] + P[\hat{\mathbf{m}} \otimes \hat{\mathbf{m}} - \hat{\boldsymbol{\ell}} \otimes \hat{\boldsymbol{\ell}}]$ where S and P are the uniaxial and biaxial order parameters, respectively, $\hat{\mathbf{n}}$ is the uniaxial director, $\{\hat{\mathbf{n}}, \hat{\mathbf{m}}, \hat{\boldsymbol{\ell}}\}$ form an orthonormal triad, and $\mathbf{I}$ is the 3×3 unit matrix. The eigenvectors of $\mathbf{Q}$ give the orientation of the nematic, i.e. the director $\hat{\mathbf{n}}$, while the eigenvalues of $\mathbf{Q}$ represent the degree of ordering in the nematic. For a uniaxial nematic, $\mathbf{Q}$ is simply $\mathbf{Q} = S[\hat{\mathbf{n}} \otimes \hat{\mathbf{n}} - (1/3)\mathbf{I}]$. The scalar S gives the local degree of ordering. $S = 0$ indicates the system is in the isotropic phase, while $S > 0$ indicates the system is in the nematic phase.

Macroscopically, a disclination line is a continuous line in which the director, $\hat{\mathbf{n}}$, is singular. Its geometry is characterized by its local tangent vector $\hat{\mathbf{T}}$ and a rotation vector $\hat{\boldsymbol{\Omega}}$. Near the singular core, $\hat{\boldsymbol{\Omega}} \cdot \hat{\mathbf{n}} = 0$ on the plane normal to $\hat{\mathbf{T}}$ [45]. That is, close to the disclination core, the director lies on a plane perpendicular to $\hat{\boldsymbol{\Omega}}$ as one encircles the core on its normal plane. Both $\hat{\mathbf{T}}$ and $\hat{\boldsymbol{\Omega}}$ may vary along the disclination, and their relationship (i.e. $\hat{\mathbf{T}} \cdot \hat{\boldsymbol{\Omega}}$) greatly affects its local motion [14,24,26]. Figure 1 illustrates director configurations on the plane normal to the line for various values of $\hat{\mathbf{T}} \cdot \hat{\boldsymbol{\Omega}}$. A few special cases referenced throughout the paper include $\hat{\mathbf{T}} \cdot \hat{\boldsymbol{\Omega}} = +1$ (a $+1/2$ wedge disclination), $\hat{\mathbf{T}} \cdot \hat{\boldsymbol{\Omega}} = -1$ (a $-1/2$ wedge disclination) and $\hat{\mathbf{T}} \cdot \hat{\boldsymbol{\Omega}} = 0$ (a twist disclination). The wedge disclination nomenclature follows from their analogue in two dimensions, thus carrying over the $+1/2$ and $-1/2$ charge in two dimensions, while the twist type disclination is named because of the characteristic twist elastic distortion present in the configuration. Even though these cases are geometrically distinct, they are all topologically equivalent (the topological charge of a disclination line in three dimensions is always 1/2). A general disclination line has $\hat{\mathbf{T}} \cdot \hat{\boldsymbol{\Omega}}$ varying along its contour. This is quite different from a dislocation in a solid, in which the topological invariant is the Burgers vector $\mathbf{b}$, constant along the line. While useful analogies

Downloaded from https://royalsocietypublishing.org/ on 06 November 2023

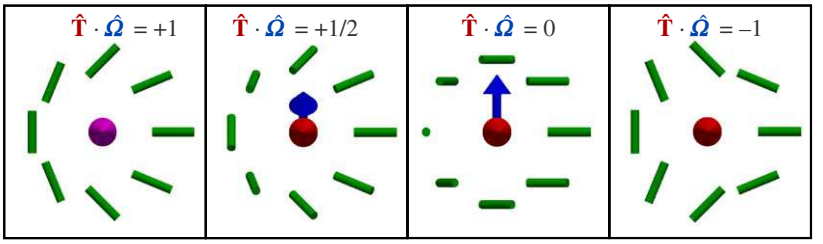

Figure 1. Examples of director configurations around disclinations with varying $\hat{\mathbf{T}} \cdot \hat{\boldsymbol{\Omega}}$. The panels indicate that a '+1/2 wedge' type disclination may be continuously rotated into a '−1/2 wedge' disclination in three dimensions. While these two configurations are topologically distinct in two dimensions, they are topologically equivalent in three dimensions.

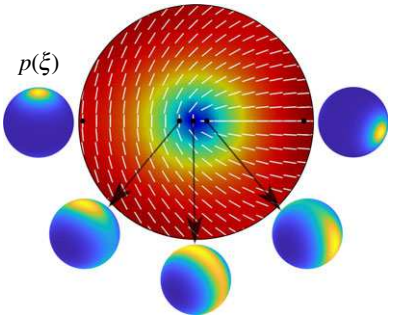

Figure 2. Computed nematogen orientational distribution, $p(\hat{\boldsymbol{\xi}})$ (equation (2.1)) at various points through a wedge disclination (colour indicates uniaxial order S, while white lines show director $\hat{\mathbf{n}}$). Far from the disclination core the distribution is uniaxial. As the core is approached the distribution becomes biaxial. At the core, the distribution is again uniaxial such that nematogens are all equally likely to lie in the plane perpendicular to $\hat{\boldsymbol{\Omega}}$. The distribution has been computed by the method of singular potentials as outlined in [48].

have been made between $\hat{\boldsymbol{\Omega}}$ and $\mathbf{b}$ [26], they are mathematically distinct, as the Burgers vector is topologically protected, and the rotation vector is not.

More microscopically, the structure of a disclination is illustrated in figure 2 which shows the probability distribution on the unit sphere at various locations in its vicinity (see §5a and the electronic supplementary material for further details). Far from the disclination, the distribution is uniaxial (fluctuations from the primary direction are isotropically distributed, and $\mathbf{Q}$ has two degenerate eigenvalues). As the core is approached, the distribution spreads out in the direction perpendicular to $\hat{\boldsymbol{\Omega}}$, becoming biaxial, so that the order parameter $\mathbf{Q}$ has three distinct eigenvalues ($P > 0$). Exactly at the core, the distribution becomes that of a disc in the plane perpendicular to $\hat{\boldsymbol{\Omega}}$. At this point, $\mathbf{Q}$ once again has two degenerate eigenvalues and so the distribution is uniaxial ($S = P$). However, the director is now perpendicular to $\hat{\boldsymbol{\Omega}}$, and $\mathbf{Q}$ describes disc like particles at the mesoscale. A subtle, but important, point is that the distribution spreads out in the plane perpendicular to $\hat{\boldsymbol{\Omega}}$. Thus the two eigenvectors corresponding to the two largest eigenvalues of $\mathbf{Q}$ are in this plane. At the core of the disclination, these two eigenvalues cross.

In addition to $\hat{\mathbf{T}}$ and $\hat{\boldsymbol{\Omega}}$, it is customary in two dimensions to define the 'orientation' of a disclination line. The orientation is the phase origin of the director as it encircles the line. In the normal plane, an angle ϕ may be defined that gives the azimuthal angle with respect to some reference axis. Further, the director at a reference angle ϕ_0 is denoted $\hat{\mathbf{n}}_0$ (see equation (3.2) for an approximate description of the director near the core). We will take $\phi_0 = 0$, and so the value of $\hat{\mathbf{n}}_0$ will describe the orientation. For example, a +1/2 disclination is in the shape of a comet (figure 1). Taking ϕ to be the angle with respect to the x-axis, $\hat{\mathbf{n}}_0 = \hat{\mathbf{x}}$ describes a +1/2 disclination

Downloaded from https://royalsocietypublishing.org/ on 06 November 2023

with the head of the comet pointing in the $-\hat{\mathbf{x}}$ direction, while $\hat{\mathbf{n}}_0 = \hat{\mathbf{y}}$ describes a $+1/2$ disclination pointing in the opposite direction. Additionally, it has been shown that the local orientation of disclination lines can be described by a series of tensors of ranks $1-3$ [26]. The rank 1 tensor gives the polarity of $+1/2$ wedge points, the rank 2 tensor gives the characteristic twist directions for a twist point, and the rank 3 tensor gives the three primary directions associated with a trifold symmetric $-1/2$ wedge point (figure 1). For an arbitrary point, all three tensors may be used to fully describe the orientation. Although this is a more mathematical method for describing the orientation of disclination lines, for this work it will only be necessary to use $\hat{\mathbf{n}}_0$ to describe disclination orientation.

3. Disclination kinematics

In a two-dimensional nematic, the order parameter $S \to 0$ as the core of a disclination is approached. This is similar to the cases of superfluids and superconductors in which the order parameter goes to zero at vortex cores [1,17,49]. However, as shown in §2, $S \neq 0$ at a disclination core in three dimensions. Instead, order goes from uniaxial to biaxial and back to uniaxial precisely at the core [46,48]. Both this lack of a singularity, and the geometric complexity of three-dimensional nematic order near disclinations, have prevented the extension of the defect tracking methods introduced by Halperin [38] and Mazenko and co-workers [39–41] to the case of three-dimensional nematics. It is shown below that such tracking methods can be introduced in this case by focusing on the line $S = P$ in which there is a crossing of eigenvalues of the tensor $\mathbf{Q}$.

Consider a system with N line disclinations, so that $\mathbf{R}_i(s)$ is the position of an element of line of the ith disclination for an arbitrary parametrization of the line. The macroscopic disclination density is [39]

$$\boldsymbol{\rho}(\mathbf{r}) = \frac{1}{2}\sum_{i}^{N} \int \frac{\mathrm{d}\mathbf{R}_i}{\mathrm{d}s}\delta[\mathbf{r} - \mathbf{R}_i(s)]\,\mathrm{d}s, \tag{3.1}$$

where the factor of $(1/2)$ arises from its topological charge, and the vector density $\boldsymbol{\rho}$ is directed along the line tangent $\hat{\mathbf{T}}$. As discussed in §2, the mesoscopic disclination core is diffuse (as also seen in experiments [50,51]), and the defect location $\mathbf{R}_i$ needs to be defined precisely. We define the location of the defect on the line $S = P$.

At the core the order parameter only has three degrees of freedom: two that define the rotation vector, $\hat{\boldsymbol{\Omega}}$, and one that indicates the strength of ordering at the core, S_C. The director deformation satisfies $\hat{\boldsymbol{\Omega}} \cdot \hat{\mathbf{n}} = 0$ on the plane normal to the disclination line [45] (close to the disclination core, the director remains in a single plane, the plane perpendicular to $\hat{\boldsymbol{\Omega}}$, as it encircles the core). Slightly away from the core on the normal plane to the line, but still within a diffuse core radius a, the order parameter is biaxial and has five degrees of freedom: three previously discussed describing the core, one for the orientation of the director (the dominant eigenvector in this biaxial region), and one for the difference between uniaxial and biaxial order, $\delta S = S - P$. In this region, the director may be written as

$$\hat{\mathbf{n}} = \hat{\mathbf{n}}_0 \cos\left(\frac{\phi - \phi_0}{2}\right) + \hat{\mathbf{n}}_1 \sin\left(\frac{\phi - \phi_0}{2}\right), \tag{3.2}$$

where $\{\hat{\mathbf{n}}_0, \hat{\mathbf{n}}_1, \hat{\boldsymbol{\Omega}}\}$ form an orthonormal triad and ϕ is the azimuthal angle in the normal plane with respect to a reference axis. Equation (3.2) is a useful approximation of the director near the core. Note that this relation is exact everywhere in the single elastic constant approximation, and for a single straight line defect with constant $\hat{\boldsymbol{\Omega}}$. In general, far-field boundary conditions, the presence of other defects, or curvature of the defect line yield more complicated director configurations,

Downloaded from https://royalsocietypublishing.org/ on 06 November 2023

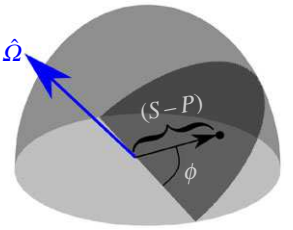

Figure 3. Schematic of the order parameter subspace near a disclination core. $\delta S = S - P$ acts as a radial coordinate while the director angle in the plane perpendicular to $\hat{\boldsymbol{\Omega}}$, ϕ, acts as an azimuthal coordinate. The transformation from real space to this subspace may be viewed as a transformation to effective polar coordinates.

especially as one moves further from the core. In the $\{\hat{\mathbf{n}}_0, \hat{\mathbf{n}}_1, \hat{\boldsymbol{\Omega}}\}$ basis, the tensor order parameter can be expressed as

$$\mathbf{Q}(0 < |\mathbf{r} - \mathbf{R}|_\perp < a) = S_C \begin{pmatrix} \frac{2}{3} & 0 & 0 \\ 0 & \frac{2}{3} & 0 \\ 0 & 0 & -\frac{4}{3} \end{pmatrix} + \delta S \begin{pmatrix} -\sin^2\frac{\phi}{2} & \frac{1}{2}\sin\phi & 0 \\ \frac{1}{2}\sin\phi & -\cos^2\frac{\phi}{2} & 0 \\ 0 & 0 & 1 \end{pmatrix} \tag{3.3}$$

where $|\mathbf{r} - \mathbf{R}|_\perp$ indicates distance in the normal plane of the disclination, and $\delta S = S - P = 0$ at the core.

Equation (3.3) defines a two-dimensional subspace schematically shown in figure 3. δS acts similarly to a radial coordinate on the subspace, while ϕ acts as an azymuth. We denote this space as $\mathbf{Q}_\perp$ as it is intuitively the part of order parameter space that is perpendicular to $\hat{\boldsymbol{\Omega}}$.

We next introduce the coordinate transformation from real space to this order parameter subspace so that the delta function in equation (3.1) may be transformed to $\delta[\mathbf{Q}_\perp]$, giving disclination locations in terms of the order parameter. To accomplish this, we first note that if $\mathbf{Q}$ is parametrized in terms of S and P, with $\hat{\mathbf{n}}$ given by equation (3.2), $\hat{\boldsymbol{\ell}} = \hat{\boldsymbol{\Omega}}$, and $\hat{\mathbf{m}} = \hat{\boldsymbol{\Omega}} \times \hat{\mathbf{n}}$, then the quantity

$$\hat{\Omega}_\gamma \varepsilon_{\gamma\mu\nu} Q_{\mu\alpha} \nabla Q_{\nu\alpha} = \frac{(\delta S)^2}{2} \nabla\phi, \tag{3.4}$$

where summation of repeated indices is assumed. We use the fact that a density $\boldsymbol{\rho} = \hat{\mathbf{z}}\delta(x)\delta(y)$ may be transformed to typical polar coordinates, (ρ, θ), such that $\boldsymbol{\rho} = \nabla \times (\rho\nabla\theta)\delta(\rho)$. Then, one may identify $(\delta S)^2/2 \equiv \rho$ and $\phi \equiv \theta$ so that the curl of equation (3.4) defines the transformation from the real space defect density to the density in order parameter space:

$$\boldsymbol{\rho}(\mathbf{r}) = \delta[\mathbf{Q}_\perp]\hat{\boldsymbol{\Omega}} \cdot \mathbf{D}(\mathbf{r}) \quad \text{and} \quad D_{\gamma i} = \varepsilon_{\gamma\mu\nu}\varepsilon_{ik\ell}\partial_k Q_{\mu\alpha}\partial_\ell Q_{\nu\alpha}. \tag{3.5}$$

This is the central result of this section that gives the transformation between the defect density in real and order parameter spaces (as indicated by the arguments of the Dirac delta functions in equations (3.1) and (3.5)). Note that in taking the curl of equation (3.4) there should be three terms. However, the term $\sim \nabla\hat{\boldsymbol{\Omega}} \times (\mathbf{Q} \times \nabla\mathbf{Q})$ goes to zero because the derivative of $\hat{\boldsymbol{\Omega}}$ is perpendicular to itself since $\hat{\boldsymbol{\Omega}}$ is a unit vector and $\mathbf{Q} \times \nabla\mathbf{Q} \propto \hat{\boldsymbol{\Omega}}$. The other term $\sim \hat{\boldsymbol{\Omega}} \cdot [\mathbf{Q} \times (\nabla \times \nabla\mathbf{Q})]$ is likewise zero since $\mathbf{Q}$ is a non-singular quantity (i.e. the curl of the gradient is zero). We also note that $\hat{\boldsymbol{\Omega}} \cdot \mathbf{D} \propto \hat{\mathbf{T}}$ [52] as required since $\boldsymbol{\rho} \propto \hat{\mathbf{T}}$.

Equation (3.5) is the analogue of the transformation used to study point and line defects in $O(n)$ n-vector models [38–41]. Defects there are identified as zeros of the n-vector order parameter $\boldsymbol{\psi}$, and the map from real space to order parameter space leads to a defect density transformation of the form

$$\rho(\mathbf{r}) = \sum_i m_i \delta(\mathbf{r} - \mathbf{r}_i) = \delta[\boldsymbol{\psi}(\mathbf{r})]D(\mathbf{r}),$$

Downloaded from https://royalsocietypublishing.org/ on 06 November 2023

where $\mathbf{r}_i$ is the location of the ith defect with charge m_i and D is the appropriate Jacobian. This formalism has been widely used to describe defects in superfluids, superconductors, XY models and classical ferromagnets, to name a few. A similar approach has been used to study dislocations in solids using a phase field model of the lattice displacement [22,43].

(a) Velocity of a disclination line

The transformation (3.5) allows the derivation of the kinematic law of motion for the disclination line. The derivation is summarized here; details can be found in the electronic supplementary material. By taking the time derivative of the left-hand side of equation (3.5), given the definition of the density in (3.1), one finds that $\partial_t \rho_i = \partial_k (v_i \rho_k - v_k \rho_i)$, where $\mathbf{v}(s) = \mathrm{d}\mathbf{R}(s)/\mathrm{d}t$ is the velocity of the line. On the other hand, the derivative of the right-hand side can be computed by explicitly obtaining the time derivative of the disclination density tensor. The following conservative form is obtained

$$\partial_t D_{\gamma i} = 2\partial_k J_{\gamma ik} \quad \text{and} \quad J_{\gamma ik} = \epsilon_{\gamma\mu\nu}\epsilon_{ikl}\partial_t Q_{\mu\alpha}\partial_l Q_{\nu\alpha},$$

where $J_{\gamma ik}$ is the disclination density current. This equation reflects the conservation of topological charge density in the normal plane of the disclination. Therefore, one finds (also using the definition of the density (3.5)) that,

$$2\hat{\Omega}_\tau J_{\tau ik}\delta[\mathbf{Q}_\perp] = \hat{\Omega}_\gamma (v_i D_{\gamma k} - v_k D_{\gamma i})\delta[\mathbf{Q}_\perp],$$

equality that applies only at the core of the disclination. This equation can be solved for the velocity by introducing an auxiliary tensor field $\mathbf{g}$, so that the velocity of a disclination line is,

$$\mathbf{v}(s) = 2\left.\frac{\hat{\mathbf{T}} \times (\hat{\boldsymbol{\Omega}} \cdot \mathbf{g})}{|\mathbf{D}|}\right|_{\mathbf{r}=\mathbf{R}(s)} \qquad g_{\gamma k} = \varepsilon_{\gamma\mu\nu}\partial_t Q_{\mu\alpha}\partial_k Q_{\nu\alpha}, \tag{3.6}$$

where the tensor field $\mathbf{g}$ is related to the topological charge current, and all quantities are computed at the disclination core. Note that the velocity is explicitly perpendicular to the tangent vector of the disclination, as expected.

Equation (3.6) is an exact kinematic relation between the velocity of a disclination line (defined as the line $S = P$) and the evolution equation of the tensor order parameter. Thus, the equation is valid for any dynamic model of nematic evolution, be it simply diffusive relaxation, involve coupling to hydrodynamic transport or be a model of an active phase. The details of the dynamic model are contained in the tensor $\mathbf{g}$, or more specifically, in its explicit dependence on $\partial_t \mathbf{Q}$. Another important property of equation (3.6) is it only needs to be computed at the disclination core. This includes both tangent and rotation vectors, $\hat{\mathbf{T}}$ and $\hat{\boldsymbol{\Omega}}$. This property will allow us to analytically predict defect motion in a variety of disclination configurations in subsequent sections by using an approximation for $\mathbf{Q}$ that is accurate close to the core.

Finally, we note that equation (3.6) reduces to the expression derived in [44] for the velocity of a disclination in a two-dimensional nematic. In that case, by taking $\hat{\mathbf{T}} = \hat{\mathbf{z}}$ and $\hat{\boldsymbol{\Omega}} = \pm\hat{\mathbf{z}}$, one finds

$$v_i = \mp 4 \frac{\varepsilon_{3ik}\varepsilon_{3\mu\nu}\partial_t Q_{\mu\alpha}\partial_k Q_{\nu\alpha}}{\varepsilon_{3\ell p}\varepsilon_{3\tau\xi}\partial_\ell Q_{\tau\beta}\partial_p Q_{\xi\beta}}. \tag{3.7}$$

4. Linear core approximation. The Peach–Koehler force

Equation (3.6) specifies the velocity of a disclination line in terms of derivatives of the order parameter only at the defect core. This is in general a complex problem that requires, in principle, the solution for the field $\mathbf{Q}$ everywhere. Considerable analytic progress can be made, however, by introducing the linear core approximation of Long *et al*. [26]. This is similar to the linear core approximations made for vortices in superfluids and superconductors, or for the motion of dislocations in solids when modelled by a phase field [22].

For the purposes of this section, when analysing an arbitrary point on a disclination line, we will adjust our axes so the point of interest is located at $\mathbf{r} = 0$ and take the azimuthal angle $\phi = 0$

Downloaded from https://royalsocietypublishing.org/ on 06 November 2023

to coincide with the positive x-axis so that the tangent vector to the disclination line is $\hat{\mathbf{T}} = \hat{\mathbf{z}}$. The linear core approximation is derived by first noting that in the uniaxial region away from the core $\mathbf{Q}$ may be written in terms of the vectors $\{\hat{\mathbf{n}}_0, \hat{\mathbf{n}}_1, \hat{\boldsymbol{\Omega}}\}$ in equation (3.2):

$$\mathbf{Q} = S_N\left[\frac{1}{6}\mathbf{I} - \frac{1}{2}\hat{\boldsymbol{\Omega}}\otimes\hat{\boldsymbol{\Omega}} + \frac{1}{2}\cos\phi(\hat{\mathbf{n}}_0\otimes\hat{\mathbf{n}}_0 - \hat{\mathbf{n}}_1\otimes\hat{\mathbf{n}}_1) + \frac{1}{2}\sin\phi(\hat{\mathbf{n}}_0\otimes\hat{\mathbf{n}}_1 + \hat{\mathbf{n}}_1\otimes\hat{\mathbf{n}}_0)\right]. \tag{4.1}$$

Inside a diffuse core of radius a, $\mathbf{Q}$ is linearly interpolated by replacing $\cos\phi \to x/a$ and $\sin\phi \to y/a$, so that $\mathbf{Q}$ near the core is approximately given by

$$\mathbf{Q} = S_N\left[\frac{1}{6}\mathbf{I} - \frac{1}{2}\hat{\boldsymbol{\Omega}}\otimes\hat{\boldsymbol{\Omega}} + \frac{x}{2a}(\hat{\mathbf{n}}_0\otimes\hat{\mathbf{n}}_0 - \hat{\mathbf{n}}_1\otimes\hat{\mathbf{n}}_1) + \frac{y}{2a}(\hat{\mathbf{n}}_0\otimes\hat{\mathbf{n}}_1 + \hat{\mathbf{n}}_1\otimes\hat{\mathbf{n}}_0)\right]. \tag{4.2}$$

As shown in [26], this approximation for $\mathbf{Q}$ is quite good near the point where the eigenvalues cross and, remarkably, it is also fully biaxial in the region $0 < \rho < a$, even though far from the core $\mathbf{Q}$ is purely uniaxial. We will use this approximation to make a number of predictions for the disclination velocity in several prototypical configurations by using it in conjunction with equation (3.6).

We focus first on simple diffusive relaxation of the tensor order parameter, $\partial_t\mathbf{Q} = -\Gamma[\delta F/\delta\mathbf{Q}]^{TS}$, where F is the free energy and $[\cdot]^{TS}$ denotes the traceless, symmetric part of a tensor. If F has a functional derivative with non-gradient terms that are analytic in $\mathbf{Q}$ at the disclination core (such as the Landau–de Gennes free energy or the model used here for numerics—see §5a and the electronic supplementary material), then the velocity of the line does not depend on those terms. This follows from $g_{\gamma k} = \varepsilon_{\gamma\mu\nu}(\mathbf{Q}^n)_{\mu\alpha}\partial_k Q_{\nu\alpha} = 0$ when computed at the core for any power n. Thus, one needs only focus on gradient terms from the elastic free energy. In the one elastic constant approximation, we may write $\partial_t\mathbf{Q} \propto \nabla^2\mathbf{Q}$ in equation (3.6). We will assume this gives the evolution of $\mathbf{Q}$ for the rest of the paper unless otherwise specified.

First, for a single, straight line disclination, equation (3.6) predicts $\mathbf{v} = 0$, since $\nabla^2\mathbf{Q} = 0$ at the core of the disclination. This is the correct stationary state for a single straight line disclination. However, as we will show, curvature in the disclination line, even if isolated, may result in a non-zero velocity.

One way to induce disclination motion is through an externally imposed distortion of the director field. The simplest case (and most relevant to interacting disclinations) is a small, non-uniform rotation of angle $\tilde{\varphi}(\mathbf{r})$ of the director field near the disclination core about an axis $\hat{\mathbf{q}}$. In this case,

$$\hat{\mathbf{n}} \to \tilde{\mathbf{n}} = \cos\tilde{\varphi}\hat{\mathbf{n}} + \sin\tilde{\varphi}(\hat{\mathbf{q}}\times\hat{\mathbf{n}}) + (1-\cos\tilde{\varphi})(\hat{\mathbf{q}}\cdot\hat{\mathbf{n}}). \tag{4.3}$$

We further assume that $\tilde{\varphi}$ is small near the core so that $\tilde{\mathbf{n}} \approx \hat{\mathbf{n}} + \tilde{\varphi}(\hat{\mathbf{q}}\times\hat{\mathbf{n}})$. We then use equation (3.2) to express $\tilde{\mathbf{n}}$ near the disclination core:

$$\tilde{\mathbf{n}} = \cos\frac{1}{2}\phi\tilde{\mathbf{n}}_0 + \sin\frac{1}{2}\phi\tilde{\mathbf{n}}_1, \tag{4.4}$$

where $\tilde{\mathbf{n}}_0$ and $\tilde{\mathbf{n}}_1$ are defined analogously to $\tilde{\mathbf{n}}$.

We now have all of the pieces of our approximations to use equation (3.6) to predict disclination motion. Combining the linear core approximation, equation (4.2), and the perturbed director near the core, equation (4.4), gives the final approximation for the perturbed $\mathbf{Q}$ near the core

$$\mathbf{Q} \approx S_N\left[\frac{1}{6}\mathbf{I} - \frac{1}{2}\hat{\boldsymbol{\Omega}}\otimes\hat{\boldsymbol{\Omega}} + \frac{x}{2a}(\tilde{\mathbf{n}}_0\otimes\tilde{\mathbf{n}}_0 - \tilde{\mathbf{n}}_1\otimes\tilde{\mathbf{n}}_1) + \frac{y}{2a}(\tilde{\mathbf{n}}_0\otimes\tilde{\mathbf{n}}_1 + \tilde{\mathbf{n}}_1\otimes\tilde{\mathbf{n}}_0)\right] \tag{4.5}$$

where $\tilde{\mathbf{n}}_i \equiv \hat{\mathbf{n}}_i + \tilde{\varphi}(\hat{\mathbf{q}}\times\hat{\mathbf{n}}_i)$.

Substituting equation (4.5) into equation (3.6) (details of this calculation are given in the electronic supplementary material) yields a simple expression for the velocity of the disclination line:

$$\mathbf{v} = -4(\hat{\mathbf{q}}\cdot\hat{\boldsymbol{\Omega}})(\hat{\mathbf{T}}\times\nabla\tilde{\varphi})|_{\rho=0}, \tag{4.6}$$

where we have expressed quantities in dimensionless units defined in §5a. In addition to giving the line velocity, it shows that, in particular, if the director is subjected to a small, *non-uniform*

Downloaded from https://royalsocietypublishing.org/ on 06 November 2023

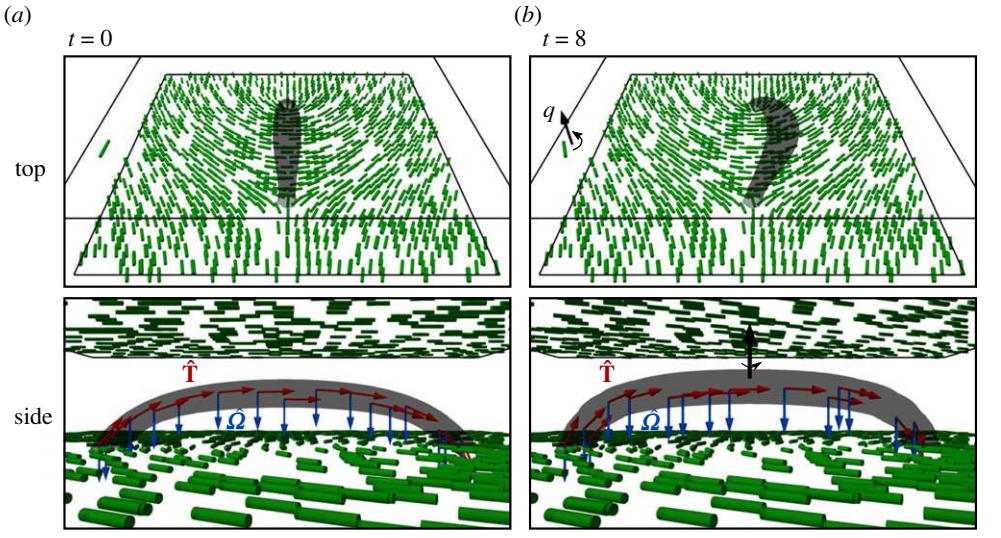

Figure 4. Disclination motion induced by externally imposed director rotation. The top row shows a top down view, while the bottom row shows a side view. (*a*) Disclination line at time $t = 0$ formed between patterned $\pm 1/2$ wedge disclinations on the bottom boundary. The top boundary has director $\hat{\mathbf{n}} = \hat{\mathbf{x}}$ fixed. (*b*) Same disclination line at $t = 8$ (computation units). For $t > 0$, the top boundary is changed to have director $\hat{\mathbf{n}} = \cos\tilde{\varphi}_0\hat{\mathbf{x}} + \sin\tilde{\varphi}_0\hat{\mathbf{y}}$ with $\tilde{\varphi}_0 = \pi/8$, simulating a rotation of the top boundary. This imposed rotation in turn imposes a stress on the configuration which results in motion of the disclination, predicted by equation (4.6). In the figures, the black arrows represent the axis of rotation $\hat{\mathbf{q}}$, the red arrows indicate the tangent vector to the disclination $\hat{\mathbf{T}}$, and the blue arrows indicate the rotation vector $\hat{\boldsymbol{\Omega}}$.

rotation, a point on a disclination line will move if $\hat{\boldsymbol{\Omega}} \cdot \hat{\mathbf{q}} \neq 0$ and if $\hat{\mathbf{T}}$ at that point is not parallel to $\nabla\tilde{\varphi}$. We note that equation (4.6) is the analogue of the Peach–Koehler relation of dislocation mechanics [15,17]. The Peach–Koehler force applied to nematic liquid crystals was first introduced by Kléman [53] and has been recently used to study disclination line motion in various scenarios [26,54]. Our analysis here using equation (3.6) represents an alternative derivation of this result that does not directly compare disclinations to dislocations in solids. Further, as we show in various examples in the next section, the above method may be generalized to obtain similar velocity equations for systems with twisted defect orientations and anisotropic elasticity, which has not been possible with the traditional application of Peach–Koehler theory to nematics [26].

We have compared the result of (4.6) with a numerical study of the motion of a disclination line between two plates with fixed nematogen orientation. The numerical details of the algorithm are given in §5a and in the electronic supplementary material. The top plate boundary condition is $\hat{\mathbf{n}} = \hat{\mathbf{x}}$, parallel to the plate, while the bottom plate boundary condition has $\hat{\mathbf{n}}$ parallel to the plate but defining a $\pm 1/2$ disclination pair. Neumann boundary conditions for the director are specified on the lateral boundaries. The system is then allowed to relax to a stable configuration in which a three-dimensional disclination line forms connecting the $+1/2$ and $-1/2$ disclinations on the bottom plate. This state is shown in figure 4*a* along with its tangent and rotation vectors at various points, which are computed from $\mathbf{D}$ [52]. After the stable state is reached, the boundary condition on the top plate is instantaneously rotated so that the director is now given by $\cos\tilde{\varphi}_0\hat{\mathbf{x}} + \sin\tilde{\varphi}_0\hat{\mathbf{y}}$, where $\tilde{\varphi}_0 = \pi/8$. This constitutes a rotation about axis $\hat{\mathbf{q}} = \hat{\mathbf{z}}$ and induces a gradient $\nabla\tilde{\varphi} \propto \hat{\mathbf{z}}$. As seen in figure 4*b*, this induces motion in the disclination line, primarily at the midpoint where $|\hat{\mathbf{T}} \times \nabla\tilde{\varphi}|$ is largest, in agreement with equation (4.6).

Downloaded from https://royalsocietypublishing.org/ on 06 November 2023

5. Analytical and numerical results

We address next how this method of analytically computing disclination velocities can be used to accurately predict the motion of multiple disclinations, as interacting disclinations behave as if they induce rotations in the local director fields of one another.

(a) Numerical algorithm

Here we briefly summarize the numerical method used in the previous and following sections. We model passive relaxation dynamics unless otherwise specified. That is, $\partial_t \mathbf{Q} = -\Gamma[\delta F/\delta \mathbf{Q}]^{TS}$ where Γ is a rotational diffusion coefficient. The free energy we choose may be written in two parts $F = \int [f_B(\mathbf{Q}) + f_e(\mathbf{Q}, \nabla \mathbf{Q})]\, \mathrm{d}\mathbf{r}$ where f_B is the bulk part of the free energy density that describes the phase behaviour of the nematic, while f_e is an elastic free energy density that penalizes spatial variations. The bulk free energy we use is based on a singular Maier–Saupe potential originally analysed by Ball and Majumdar and recently developed computationally [47,48,55],

$$f_B(\mathbf{Q}) = -\kappa\, \mathrm{Tr}[\mathbf{Q}^2] - T\Delta s \quad \text{and} \quad \Delta s = -nk_B \int_{\mathcal{S}^2} p(\hat{\boldsymbol{\xi}}) \ln 4\pi p(\hat{\boldsymbol{\xi}})\, \mathrm{d}\Sigma(\hat{\boldsymbol{\xi}}) \tag{5.1}$$

where κ is a phenomenological interaction coefficient, Δs is the entropy density relative to the isotropic phase, n is the number density of nematogens, k_B is the Boltzmann constant, and $p(\hat{\boldsymbol{\xi}})$ is the constant temperature, orientational probability distribution. Note that the integral in Δs is over the unit sphere.

For the elastic free energy density, we use

$$f_e(\mathbf{Q}, \nabla \mathbf{Q}) = L_1 \partial_k Q_{ij} \partial_k Q_{ij} + L_2 \partial_j Q_{ij} \partial_k Q_{ik} + L_3 Q_{k\ell} \partial_k Q_{ij} \partial_\ell Q_{ij}, \tag{5.2}$$

where L_i are elastic coefficients. For a uniaxial nematic, comparison of equation (5.2) and the Frank–Oseen elastic free energy yields a mapping to the splay (K_{11}), twist (K_{22}) and bend (K_{33}) coefficients [56–58]. The one constant approximation ($K_{11} = K_{22} = K_{33}$) may be achieved by setting $L_2 = L_3 = 0$. Note that $L_3 \neq 0$ is required to break the degeneracy $K_{11} = K_{33}$.

Equation (5.1) with a specific form of $p(\hat{\boldsymbol{\xi}})$ constrains $\mathbf{Q}$ to be given by equation (2.1) [47,48,55]. Because the Landau–de Gennes free energy is unbounded for elastic energies cubic in $\mathbf{Q}$, this specific choice of bulk free energy makes the case of a nematic with anisotropic elasticity numerically tractable [48,55,57]. In some of the presented cases, we will use the one constant approximation, and so the use of this free energy is not strictly necessary. In these cases, our qualitative results should be reproducible with a more common Landau–de Gennes free energy functional instead. The electronic supplementary material provides details about the computational implementation of equation (5.1).

In all cases, we solve the equations of motion for $\mathbf{Q}$ by discretizing in space on a square (two-dimensional) or cube (three-dimensional) that is meshed with triangles or tetrahedra. We discretize in time by using a semi-implicit convex splitting algorithm [59–61]. The discretized matrix equations are then solved using the Matlab/C++ package FELICITY [62] and the multigrid matrix equation solver AGMG [63–66]. For all problems, we use Neumann boundary conditions unless otherwise specified.

Finally, all lengths are made dimensionless by the nematic correlation length $\xi = \sqrt{L_1/(nk_BT)}$, energies by $\xi^3 nk_BT$, and times by the nematic relaxation time scale $\tau = 1/(\Gamma \xi^3 nk_BT)$. For all computations, we set $L_1 = 0.5$ and $\Gamma = 1$ which set the length and time scale. This leaves the following dimensionless parameters for the system: $\kappa/(nk_BT)$, $\tilde{L}_2 = L_2/L_1$ and $\tilde{L}_3 = L_3/L_1$. We will always set $\kappa/(nk_BT) = 4$, which corresponds to a system in the nematic phase with $S_N = 0.6751$ [47], and we subsequently drop the tilde on L_2 and L_3.

(b) Twisted defects in two dimensions

We first present results that apply to disclination pairs in two-dimensional systems. These systems have been thoroughly studied [19,21,29,67–69], and as such, the results presented here are not

Downloaded from https://royalsocietypublishing.org/ on 06 November 2023

new, but rather a reinterpretation and alternative derivation of previous results. We will also use the simpler two-dimensional case to demonstrate how we apply equation (4.6) to systems of interacting disclinations.

In two dimensions, the director can be defined by its angle relative to the x-axis, ϕ. In a system with N disclinations, ϕ is given by

$$\phi(x,y) = \sum_{i=1}^{N} m_i \arctan\left(\frac{y-y_i}{x-x_i}\right) + \phi_0, \tag{5.3}$$

$m_i = \pm 1/2$ is the charge of the ith disclination, (x_i, y_i) is the position of the ith disclination, and ϕ_0 is an overall phase factor determined by the orientations of all the defects. Equation (5.3) minimizes the one elastic constant Frank–Oseen free energy for a system constrained to have N disclinations at points (x_i, y_i).

Note that, as disclinations are added to the system, the effect is to add a non-uniform rotation everywhere outward from the centre of the disclination. From the perspective of the jth disclination, the rest of the disclinations add small, rotatory perturbations. Hence, we identify the field $\tilde{\varphi}$ in equation (4.6) with $\phi(x,y) - \phi_j(x,y)$ where $\phi_j(x,y)$ is the angle of the director that is attributed only to the jth disclination. Then, using the two-dimensional version of equation (4.6), the velocity of the jth disclination in a two-dimensional system of N disclinations is

$$\mathbf{v}_j = 8 \sum_{i \neq j} m_i \frac{\mathbf{R}_j - \mathbf{R}_i}{|\mathbf{R}_j - \mathbf{R}_i|^2}, \tag{5.4}$$

where $\mathbf{R}_i = (x_i, y_i)$. Equation (5.4) is the well-known 'Coulomb-like' interaction between disclinations in a nematic [29]. Equation (5.4) is traditionally derived by using the Frank–Oseen free energy, written in terms of disclination positions. The disclination kinematic law is an alternative method of deriving the same result.

Now consider the case of two oppositely charged disclinations. Equation (5.4) shows that the disclinations will annihilate moving along the line connecting the two disclination cores. Recently, the Frank–Oseen free energy has been minimized for the case of two disclinations fixed in space, but having arbitrary relative orientation $\delta\phi$ [21]. Figure 5*a* shows the director field for the standard case in which the orientation between disclinations is 'optimal' ($\delta\phi = 0$), whereas figure 5*b* shows the case of 'twisted' disclinations in which $\delta\phi = \pi$. One may think of this configuration as being formed by 'twisting' one of the disclinations by an angle $2\delta\phi$ relative to the other. Tang & Selinger [21] showed that in the twisted case, and for defects sufficiently separated, the director angle is given by

$$\begin{aligned}\phi(x,y) = {} & \frac{1}{2}\arctan\left(\frac{y-y_1}{x-x_1}\right) - \frac{1}{2}\arctan\left(\frac{y-y_2}{x-x_2}\right) \\ & + \frac{\delta\phi}{2}\left[1 + \frac{\ln(|\mathbf{r}-\mathbf{R}_1|^2) - \ln(|\mathbf{r}-\mathbf{R}_2|^2)}{\ln(|\mathbf{r}_1-\mathbf{r}_2|^2) - \ln(a^2)}\right] + \phi_0,\end{aligned} \tag{5.5}$$

where a is the disclination core radius. If $\delta\phi = 0$, this case reduces to the optimal orientation case. The Frank–Oseen interaction energy of this configuration in terms of the distance between disclinations, $R = |\mathbf{R}_1 - \mathbf{R}_2|$, and the 'twistedness' $\delta\phi$ of the configuration is [21],

$$\Delta F_{\mathrm{FO}} = \frac{\pi K}{2}\ln\left(\frac{R}{a}\right) + \frac{\pi K \delta\phi^2}{2}\frac{\ln[R/(2a)]}{\ln[R/a]^2}, \tag{5.6}$$

where K is the Frank–Oseen elastic constant in the one-constant approximation. Importantly, the energy only depends on the distance between the disclinations and the twistedness of the configuration. Thus, the effective force (computed from this energy) that one disclination exerts on the other is directed along the line segment that joins them.

The disclinations, however, follow a more complex trajectory. As studied in [21,68,69], disclinations in twisted configurations have velocities with components transverse to the line segment that joins them. We show in figure 6 a few example trajectories numerically obtained. As

Downloaded from https://royalsocietypublishing.org/ on 06 November 2023

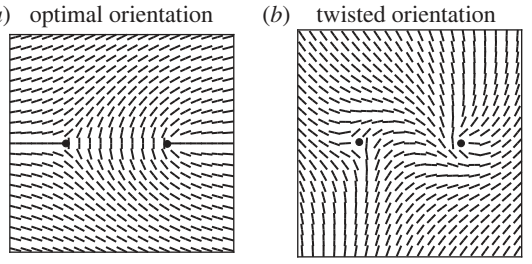

Figure 5. (*a*) Director configuration for two oppositely charged two-dimensional disclinations with 'optimal' orientation. (*b*) Director configuration for two oppositely charged two-dimensional disclinations with 'twisted' orientation. The angle between orientations $\delta\phi = \pi$.

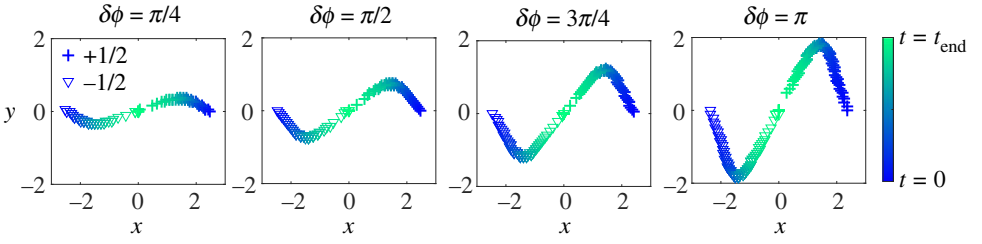

Figure 6. Trajectories of twisted disclinations for difference in orientations $\delta\phi = \pi/4,\ \pi/2,\ 3\pi/4,\ \pi$. As $\delta\phi$ increases, the trajectories become more transverse. The transverse trajectories cannot be predicted from the energy of the configuration, yet the application of the kinematic velocity equation, equation (5.7), qualitatively captures the motion. In the figures, + symbols represent the positions of the +1/2 disclination, while triangles represent the positions of −1/2 disclinations. For each case, the colouring indicates the time and is scaled from $t = 0$ to $t = t_{\text{end}}$, the time at which the disclinations annihilate, which increases as $\delta\phi$ increases.

the initial $\delta\phi$ is increased, the trajectories become more transverse, and straight line annihilation occurs only after the twisted distortion between the disclinations vanishes. Intuitively, the motion is due to a restoring torque, which drives the disclinations to rotate back to the optimal orientation. One way to rotate a disclination is by uniformly rotating all of the nematogens in the system. However, a uniform rotation in a system with two disclinations would only rotate both disclinations in the same direction, and hence would not reduce the relative twistedness between disclinations. Thus, the nematogens must rotate locally, near each defect inhomogeneously. The only way this can be accomplished while maintaining continuity in the director field (at all points except the disclinations) is by moving the disclinations transverse to one another.

This disclination behaviour cannot be understood from the effective force resulting from equation (5.6). Instead, the kinematic law, equation (3.6), can be used with $\tilde{\varphi} = \phi - \phi_1^{\text{singular}}$ where ϕ_1^{singular} is the part of equation (5.5) that is singular at $\mathbf{R}_1$. The predicted velocity of disclination 1 is

$$\mathbf{v}_1 = -2\left[\frac{1}{R}\hat{\mathbf{R}}_{12} - \frac{\delta\phi}{R\ln(R/a)}(\hat{\mathbf{z}} \times \hat{\mathbf{R}}_{12})\right], \tag{5.7}$$

where $\hat{\mathbf{R}}_{12} = (\mathbf{R}_1 - \mathbf{R}_2)/R$. The second term in equation (5.7) is a transverse contribution that is proportional to $\delta\phi$. If $\delta\phi = 0$, the standard motion for optimally orientated disclinations follows. The velocity of disclination 2 may also be derived in a similar manner and is precisely opposite to that of equation (5.7).

That the kinematic law gives a qualitatively correct velocity for twisted disclinations, whereas an over damped velocity proportional to the driving force does not, implies a tensorial effective mobility linking velocity and driving force that is of topological origin. From the perspective of

Downloaded from https://royalsocietypublishing.org/ on 06 November 2023

the nematogens, the motion is geometrically constrained: nematogens must rotate locally while the director field remains continuous, and the only way to accomplish this is for the disclinations to move in the transverse direction. From the alternative perspective of defects being the primary dynamical objects, one may interpret this motion as a topological constraint that must be obeyed while energy minimization drives the relaxation.

(c) Defect motion in two-dimensional elastically anisotropic media

We now consider two disclinations optimally oriented (not twisted relative to one another), though we relax the one constant approximation so that $K_{11} \neq K_{33}$. The director field around a single disclination when $K_{11} \neq K_{33}$ is known [51,70,71]. However, for configurations involving two or more disclinations, the single defect solutions may not be simply superimposed because the Euler–Lagrange equations determining free energy minima are no longer linear [72]. Therefore, unlike the case of isotropic elasticity, the free energy cannot be computed analytically. The effect of one disclination on the other will be described by an unknown, local, inhomogeneous rotation of the director. From equation (3.6) for the case of anisotropic elasticity (we assume $L_3 \neq 0$), the contribution to the dynamics of $\mathbf{Q}$ from the elastic free energy, equation (5.2), is

$$\partial_t Q_{\mu\nu} = \nabla^2 Q_{\mu\nu} + L_3(-\partial_\mu Q_{ij}\partial_\nu Q_{ij} + 2\partial_i Q_{\mu\nu}\partial_j Q_{ij} + 2Q_{ij}\partial_\mu\partial_\nu Q_{ij})^{TS}. \tag{5.8}$$

We now compute the velocity of the $+1/2$ disclination, disclination 1, by noting that the director is rotated by a field $\tilde{\varphi}_2$, that is, the rotation from equilibrium caused by disclination 2, the $-1/2$ disclination. We assume the same linear core approximation presented in §4, though the form of $\tilde{\varphi}_2$ is not known. Then by using the methods of §4, only the second term in the parentheses of equation (5.8) gives a non-zero velocity for disclination 1,

$$\mathbf{v}_1 = 4(\hat{\mathbf{z}} \times \nabla\tilde{\varphi}_2) - \frac{2S_N L_3}{a}[\hat{\mathbf{x}}\cos 2\phi_0 + \hat{\mathbf{y}}\sin 2\phi_0], \tag{5.9}$$

where ϕ_0 is the overall phase of the configuration, defined in equation (5.3). The term proportional to L_3 does not depend on $\nabla\tilde{\varphi}_2$ within the linear core approximation, but depends instead on the orientation of the disclination through ϕ_0. Of additional interest is in the computation of $\mathbf{v}_2$:

$$\mathbf{v}_2 = 4(\hat{\mathbf{z}} \times \nabla\tilde{\varphi}_1), \tag{5.10}$$

where $\tilde{\varphi}_1$ is the perturbation of the director from disclination 1. Note that there are no terms proportional to L_3.

Equations (5.9) and (5.10) predict asymmetric motion of $\pm 1/2$ disclinations when $K_{11} \neq K_{33}$. Such asymmetric motion has been observed in previous numerical work [67]. Additionally, the velocity equation reveals multiple sources of asymmetry. There is an explicit asymmetry in which the $+1/2$ disclination shows a biased motion towards its bend region if $L_3 > 0$ or towards its splay region if $L_3 < 0$. The $-1/2$ disclination shows no such bias, as expected, since it is not polar. However, there is also an implicit asymmetry, since in general $\nabla\tilde{\varphi}_1 \neq -\nabla\tilde{\varphi}_2$, unlike the case for pairs of disclinations in the one-constant approximation in which $\nabla\tilde{\varphi}_1 = -\nabla\tilde{\varphi}_2$.

We have compared these results to a numerical solution of the time evolution of the $\mathbf{Q}$-tensor in which the system is initialized with two oppositely charged disclinations. For the computations, we set $L_3 = 3$ and $\Delta t = 0.2$. We perform computations for two different cases, $\phi_0 = 0$ and $\phi_0 = \pi/2$. Figure 7 shows plots of the position x and x^2, as a function of time for the $+1/2$ and $-1/2$ disclinations for both anisotropic cases, as well as the case of an elastically isotropic system ($L_3 = 0$) for reference. We find that for $\phi_0 = 0$, the $+1/2$ disclination moves faster than the $-1/2$ disclination while the opposite occurs for the case $\phi_0 = \pi/2$. This is in agreement with equation (5.9). Additionally, the total time of annihilation is much smaller for the $\phi_0 = 0$ case than the $\phi_0 = \pi/2$ case. Further, the plots of x^2 are nonlinear for the anisotropic cases, which is in contrast to the case with isotropic elasticity when the velocity is given by equation (5.4). The difference in disclination annihilation times can be understood by noticing that the $\phi_0 = 0$ configuration has bend deformation between the two disclinations and, hence, this configuration annihilates faster

Downloaded from https://royalsocietypublishing.org/ on 06 November 2023

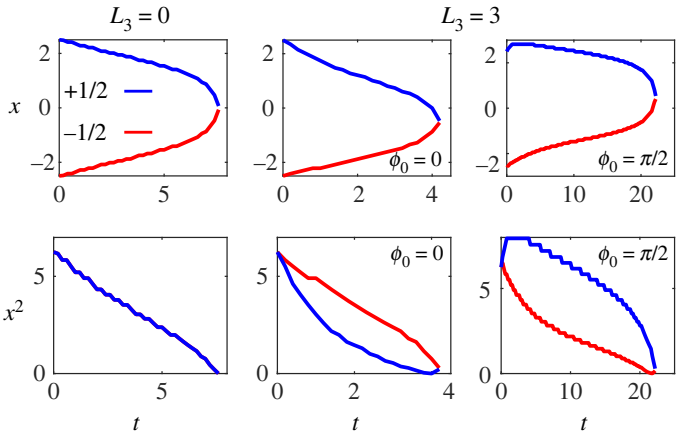

Figure 7. $\pm 1/2$ disclination positions x and x^2 versus time t in computational units for $L_3 = 0$ and $L_3 = 3$. The case $L_3 = 3$ is further differentiated by initial conditions: $\phi_0 = 0$ and $\phi_0 = \pi/2$. When $L_3 > 0$ the bend elastic constant is larger than splay, leading to an asymmetry in $\pm 1/2$ disclination motion.

to remove the bend deformation, as the bend constant is larger than the splay constant when $L_3 > 0$. On the other hand, the $\phi_0 = \pi/2$ configuration contains splay between the disclinations resulting in slower motion. However, this intuitive argument does not account for asymmetry in disclination motion, which is accounted for qualitatively by equations (5.9) and (5.10).

(d) Disclination line interaction

We turn our attention next to disclination lines in three dimensions with motion driven by their mutual interaction. It is not possible to evaluate the energy of configurations with many disclinations. Indeed, what constitutes an allowable configuration of many disclination lines remains an open question. Nevertheless, we analyse two simple, yet interesting configurations: disclination line recombination, and disclination loop self-annihilation.

(i) Line recombination

Disclination line recombination occurs when two disclinations meet at a point. They annihilate at this point and then continue to annihilate as separate lines. Here we calculate the velocity of disclination lines in a system of two straight lines with arbitrary tangent and rotation vectors. We set our coordinates so disclination 1 is located at $\mathbf{R}_1(z) = (-R/2, 0, z)$ with tangent vector $\hat{\mathbf{T}}_1 = \hat{\mathbf{z}}$. We further orient the coordinate system so that the closest point between the disclination lines lies on the x-axis and the tangent vector of disclination 2 lies in the yz-plane so that $\mathbf{R}_2(z) = (R/2, |\hat{\mathbf{z}} \times \hat{\mathbf{T}}_2|z, (\hat{\mathbf{z}} \cdot \hat{\mathbf{T}}_2)z)$. The rotation vectors are assumed to be constant along the straight lines, but are otherwise arbitrary. Note that we use the coordinate z as the parameter for both disclination lines.

Unlike in two dimensions, an equation for the exact director field for multiple disclination lines is not known due to the nonlinearity of the Frank–Oseen free energy in three dimensions [56,58]. However, we assume again that each disclination rotates the director field in its normal plane about its rotation vector, $\hat{\boldsymbol{\Omega}}$, and we can thus estimate the effect of one disclination on the other's local director field. To do this, we define two fields, $\phi_1(x, y, z)$ and $\phi_2(x, y, z)$ which give the azimuthal angle with respect to the normal planes of disclinations 1 and 2. We assume that ϕ_1 and ϕ_2 are both zero along the line segment that connects the nearest point of the disclination lines and that the disclination lines share $\hat{\mathbf{n}}_0$ so that $\hat{\boldsymbol{\Omega}}_1 \cdot \hat{\mathbf{n}}_0 = \hat{\boldsymbol{\Omega}}_2 \cdot \hat{\mathbf{n}}_0 = 0$. We show a schematic of this configuration in figure 8.

To compute the velocity of disclination 1 using equation (3.6), we assume the director field near disclination 1 is given by a small rotation of the director about the axis $\hat{\boldsymbol{\Omega}}_2$. This allows us to

Downloaded from https://royalsocietypublishing.org/ on 06 November 2023

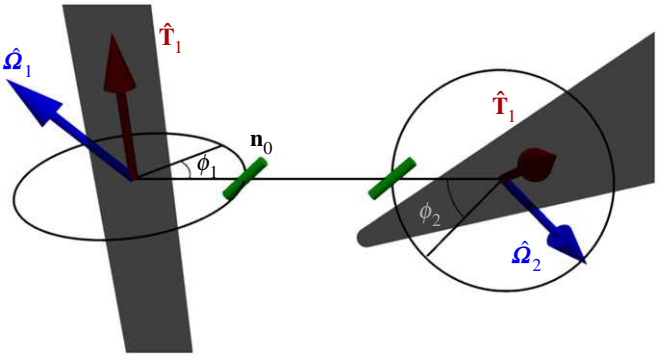

Figure 8. Schematic of the configuration for two straight line disclinations with constant rotation vectors $\hat{\boldsymbol{\Omega}}$. ϕ_1 and ϕ_2 are the azimuthal angles around each disclination defined such that $\phi_1 = \phi_2 = 0$ along the line segment that connects the closest points of the disclinations. The configuration is assumed to be such that $\hat{\mathbf{n}}_0$ is the same for both disclinations.

apply equation (4.6) near the disclination with $\tilde{\varphi} = (1/2)\phi_2$ and $\hat{\mathbf{q}} = \hat{\boldsymbol{\Omega}}_2$. This gives the velocity of disclination 1 as a function of z,

$$\mathbf{v}_1(z) = -2(\hat{\boldsymbol{\Omega}}_1 \cdot \hat{\boldsymbol{\Omega}}_2)\left[\frac{|\hat{\mathbf{T}}_1 \times \hat{\mathbf{T}}_2|z}{R^2 + |\hat{\mathbf{T}}_1 \times \hat{\mathbf{T}}_2|^2 z^2}\hat{\mathbf{y}} + \frac{(\hat{\mathbf{T}}_1 \cdot \hat{\mathbf{T}}_2)R}{R^2 + |\hat{\mathbf{T}}_1 \times \hat{\mathbf{T}}_2|^2 z^2}\hat{\mathbf{x}}\right]. \tag{5.11}$$

Equation (5.11) gives several qualitative predictions about the motion of recombining disclination lines. First, the velocity is largest at $z = 0$, the closest point between the lines, and this point moves along the line segment connecting the closest points of the disclinations. Additionally, if the lines are not parallel, then there is a component of the velocity for points $z \neq 0$ that is transverse to the direction between disclinations. This component is odd in z, and thus indicates that non-parallel lines will rotate to become parallel.

If we focus on the point $z = 0$ we find

$$\mathbf{v}_1(0) = 2(\hat{\boldsymbol{\Omega}}_1 \cdot \hat{\boldsymbol{\Omega}}_2)(\hat{\mathbf{T}}_1 \cdot \hat{\mathbf{T}}_2)\frac{\hat{\mathbf{R}}_{12}}{R}, \tag{5.12}$$

so that the closest point does not move if the tangent vectors *or* rotation vectors are perpendicular to each other. This motion of the closest points between disclination lines was analysed numerically in a previous work by us [52], and it was found that equation (5.12) for the velocity of the closest points correctly predicts the scaling of numerical computations of annihilating disclinations. Further, we note that equation (5.12) is proportional to the force between two disclinations derived in [21] by using an effective Peach–Koehler force between disclinations. Here, however, we do not integrate the force between two disclinations as is done in that work. Instead, equation (5.11) gives the velocity at all points along the disclination, predicting a non-uniform, rotating, motion.

We now expand upon our previous analysis by developing a simpler model for the time evolution of two important variables in the system: the distance between disclinations at their closest point, R, and the angle between tangent vectors at their closest point, ψ. That the disclinations rotate is important to their dynamics, since this rotation speeds them up as time goes on. Using equation (5.11) as well as the velocity for disclination 2, which can be derived in a similar manner to the velocity of disclination 1, we derive an equation for the time evolution of R by noting that $\mathrm{d}R/\mathrm{d}t = (\mathbf{R}_1 - \mathbf{R}_2) \cdot (\mathbf{v}_1 - \mathbf{v}_2)/R$. Additionally, the time evolution of ψ may be derived as follows:

$$\frac{\mathrm{d}}{\mathrm{d}t}(\hat{\mathbf{T}}_1 \cdot \hat{\mathbf{T}}_2) = \frac{\mathrm{d}}{\mathrm{d}t}\cos\psi \Leftrightarrow \frac{\mathrm{d}\hat{\mathbf{T}}_1}{\mathrm{d}t} \cdot \hat{\mathbf{T}}_2 + \hat{\mathbf{T}}_1 \cdot \frac{\mathrm{d}\hat{\mathbf{T}}_2}{\mathrm{d}t} = -\sin\psi\frac{\mathrm{d}\psi}{\mathrm{d}t}$$

Downloaded from https://royalsocietypublishing.org/ on 06 November 2023

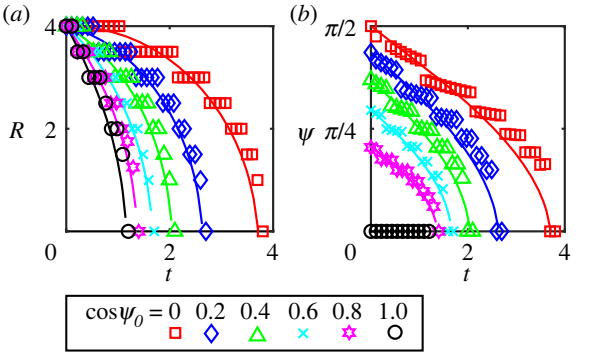

Figure 9. Disclination separation R (*a*) and angle between tangent vectors ψ (*b*) at the closest points between disclinations versus time during disclination recombination for several initial angles between disclinations. For all computations, the initial distance between disclinations is $R_0 = 4$. The points are data from **Q**-tensor computations using the model of §5 while the solid lines represent numerical solutions to equations (5.13). The time in the numerical solutions to equations (5.13) is scaled so that the annihilation coincides with that of the **Q**-tensor computations.

with

$$\frac{\mathrm{d}\hat{\mathbf{T}}_i}{\mathrm{d}t} = \frac{\mathrm{d}}{\mathrm{d}t}\frac{\mathrm{d}\mathbf{R}_i}{\mathrm{d}z} = \frac{\mathrm{d}\mathbf{v}_i}{\mathrm{d}z}.$$

Our simpler model for the dynamics of the closest points between disclinations is then given by two coupled, first-order, differential equations

$$\frac{\mathrm{d}R}{\mathrm{d}t} = \frac{4(\hat{\boldsymbol{\Omega}}_1 \cdot \hat{\boldsymbol{\Omega}}_2)\cos\psi}{R} \quad \text{and} \quad \frac{\mathrm{d}\psi}{\mathrm{d}t} = \frac{4(\hat{\boldsymbol{\Omega}}_1 \cdot \hat{\boldsymbol{\Omega}}_2)\sin\psi}{R^2}. \tag{5.13}$$

Equations (5.13) are, of course, an approximation that assumes (among others) that the disclinations remain straight, which is not the case in experiments and numerical calculations [52,73]. Nevertheless, we note a few key predictions they make. First, as previously noted, if the rotation vectors are perpendicular, there should be no motion between the disclination lines, which has been predicted and found numerically previously [26,52]. Further, if the disclinations are perpendicular and $\cos\psi = 0$ the distance between disclinations does not change. However, this does not mean that the disclinations do not move since, in this case, $\sin\psi = 1$ and so ψ changes and the disclinations rotate. Additionally, the rotation rate is proportional to $1/R^2$ and so this rotation may take much longer if the disclinations are initially far apart.

We numerically solve equations (5.13) by using a simple forward Euler method in which we take the time step $\Delta t = 0.1$, and we assume $\hat{\boldsymbol{\Omega}}_1 \cdot \hat{\boldsymbol{\Omega}}_2 = -1$. We compare these solutions against full **Q**-tensor computations of the model given in §5, setting $L_2 = L_3 = 0$ and $\Delta t = 0.1$. The three-dimensional computations were performed on a standard tetrahedral mesh with $41 \times 41 \times 41$ vertices. In the computations, we set $\hat{\boldsymbol{\Omega}}_1 = \hat{\mathbf{z}}$ and $\hat{\boldsymbol{\Omega}}_2 = -\hat{\mathbf{z}}$ and initialize the system so the initial distance between disclinations is $R_0 = 4$ with a range of initial tangent vectors so that $\cos\psi_0 \in [0, 1]$. We track the tangent vectors of the disclinations using the **D** tensor [52]. In figure 9, we plot R and ψ as a function of time for each initial condition used. In the plots, the solid lines are the Euler solutions to equations (5.13) while the points are determined from the **Q**-tensor computations. The jumps in data from the computations stem from the finite step-size of the mesh.

The solid lines in figure 9 are not fits to the computational data; however, the time is scaled so that the solutions of the model annihilate at the same time as the **Q**-tensor computations. We find excellent agreement between the two methods, which highlights the power of the kinematic equation for disclinations in analysing and predicting disclination motion since the differential equations (5.13) are much simpler, and faster to solve. We also note that the results of Long *et al*. [26] predict that the force between two perpendicular disclinations should be zero, yet we

Downloaded from https://royalsocietypublishing.org/ on 06 November 2023

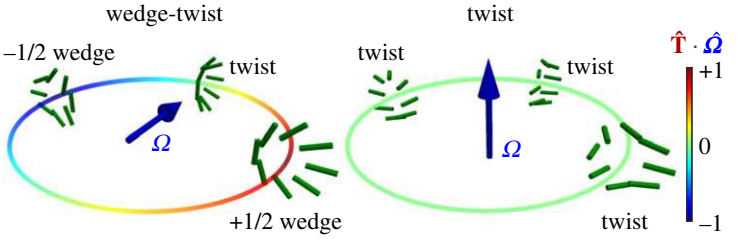

Figure 10. Sketches of wedge-twist and twist loop disclinations. The colour indicates $\hat{\boldsymbol{\Omega}} \cdot \hat{\mathbf{T}}$ along the loop while the cylinders depict the director at various points along the loop. These points are labelled by the type of elastic distortion present.

find computationally, and predict analytically, that disclinations should still eventually annihilate due to a restoring torque between non-parallel disclinations.

(ii) Loop self-annihilation

We now study the self-annihilation of initially circular disclination loops in nematics. Axes are oriented so the centre of the loop is at the origin and the loop lies in the xy-plane. We then work in standard cylindrical coordinates. Here we focus on disclination loops in which the rotation vector $\hat{\boldsymbol{\Omega}}$ is constant throughout. These are the so-called 'neutral' disclination loops such that their total point defect charge is zero [14,29]. Thus, they may self-annihilate to leave behind a uniform, defect-free, nematic texture. Additionally, there are two primary, geometric classifications of neutral disclination loops: 'twist' disclinations in which $\hat{\boldsymbol{\Omega}}$ is perpendicular to the plane of the loop and hence $\hat{\boldsymbol{\Omega}} \cdot \hat{\mathbf{T}} = 0$ everywhere; and 'wedge-twist' disclinations in which $\hat{\boldsymbol{\Omega}}$ lies in the plane of the loop and $\hat{\boldsymbol{\Omega}} \cdot \hat{\mathbf{T}} \in [-1, 1]$ changes continuously along the loop. Sketches of both configurations are given in figure 10.

To approximate $\mathbf{Q}$ near the core, we assume the director in each normal plane of the loop is given by

$$\hat{\mathbf{n}} = \cos\left(\frac{1}{2}\phi_1 + \frac{1}{2}\phi_2\right)\hat{\mathbf{n}}_0 + \sin\left(\frac{1}{2}\phi_1 + \frac{1}{2}\phi_2\right)\hat{\mathbf{n}}_1, \tag{5.14}$$

where

$$\phi_1(\rho, \theta, z) = \arctan\left(\frac{z}{R-\rho}\right) \quad \text{and} \quad \phi_2(\rho, \theta, z) = \arctan\left(\frac{z}{R+\rho}\right),$$

where R is the loop radius, and ϕ_2 represents the rotation of the director field from the opposite side of the loop. We note that this director approximation is just the rotation of the two-dimensional two defect solution about the z-axis. The introduction of cylindrical coordinates slightly modifies the linear approximation of $\mathbf{Q}$ near the disclination core, which is now given by

$$\mathbf{Q} \approx S_N\left[\frac{1}{6}\mathbf{I} - \frac{1}{2}\hat{\boldsymbol{\Omega}} \otimes \hat{\boldsymbol{\Omega}} + \frac{R-\rho}{2a}(\tilde{\mathbf{n}}_0 \otimes \tilde{\mathbf{n}}_0 - \tilde{\mathbf{n}}_1 \otimes \tilde{\mathbf{n}}_1) + \frac{z}{2a}(\tilde{\mathbf{n}}_0 \otimes \tilde{\mathbf{n}}_1 + \tilde{\mathbf{n}}_1 \otimes \tilde{\mathbf{n}}_0)\right], \tag{5.15}$$

where $\tilde{\mathbf{n}}$ is defined as in §4 and $\tilde{\varphi} = \phi_2$. In order to use the kinematic law, equation (3.6), to obtain the velocity of the disclination loop, we cannot just apply equation (4.6) since the loop is not straight, and the curvature of the loop will add to the velocity (i.e. $\nabla^2\rho \neq 0$, etc.). Using the same method as laid out in §4 and taking the tangent vector to the loop to be $\hat{\mathbf{T}} = \hat{\boldsymbol{\theta}}$ we find that the velocity is

$$\mathbf{v} = -\frac{3}{2R}\hat{\boldsymbol{\rho}}. \tag{5.16}$$

The velocity in equation (5.16) does not depend on the rotation vector $\hat{\boldsymbol{\Omega}}$. This is expected since, within the one-constant approximation, the Frank–Oseen free energy of a disclination loop does not depend on $\hat{\boldsymbol{\Omega}}$. Additionally, the velocity predicts that the loop shrinks at the same rate everywhere until it annihilates itself. The radius of the loop is predicted to scale as $R^2 \sim -t$

Downloaded from https://royalsocietypublishing.org/ on 06 November 2023

which was checked numerically in a previous work and has been observed in experiments [52,73]. We reiterate that this method does not require an integration about the loop to predict the velocity. Rather we simply approximate the configuration $\mathbf{Q}$ at points along the loop. Finally, we note in a previous analysis, [52], we did not include the contribution of $\tilde{\varphi} = \phi_2$ to the velocity (i.e. interaction with the opposite side of the loop) and only included the contribution due to disclination curvature. When including the contribution of ϕ_2, the velocity is predicted to be larger by a factor of 3/2. Further, comparing to equations (5.13) for the case of parallel disclinations, a loop of diameter equal to the distance between disclinations is predicted to annihilate in 2/3 the amount of time. Comparing $\mathbf{Q}$ tensor computations of disclination lines and loops shows that parallel disclinations initially separated by $R_0 = 5$ annihilate in 21 time-steps ($\Delta t = 0.1$), while a loop disclination with initial diameter $2R_0 = 5$ annihilates in 12 time-steps which is close to the factor of 2/3 predicted by the equations.

We conclude this section with one more example of a self-annihilating disclination loop. We consider anisotropic elasticity and set $L_2 > 0$ to describe the experimentally relevant case of larger (but still equal) bend and splay elastic constants relative to the twist constant [56–58]. With $L_2 \neq 0$ in equation (5.2), the assumed time dependence of $\mathbf{Q}$ will change. We find now

$$\partial_t Q_{ij} = \partial_k \partial_k Q_{ij} + L_2(\partial_i \partial_k Q_{jk})^{TS}. \tag{5.17}$$

In computing the velocity via the kinematic equation, we now choose a specific $\hat{\boldsymbol{\Omega}} = \hat{\mathbf{x}}$. Owing to elastic anisotropy, the velocity will depend on the director configuration of the loop. If the disclination is a twist loop, the elastic deformation around the loop is the same at each point. In this case, the disclination will still have an isotropic velocity. Instead we focus on the case of a wedge-twist loop in which $\pm 1/2$ wedge and twist-type deformations are represented along the loop (figure 10).

For a circular wedge-twist loop disclination with $L_2 \neq 0$, we find that the velocity of the loop is

$$\mathbf{v}(\theta) = -\frac{1}{2R}[3 + \frac{L_2}{4}(4 + 4\cos^2\theta - 2\sin\theta)]\hat{\boldsymbol{\rho}}, \tag{5.18}$$

where θ is the azimuthal angle with respect to the x-axis. For the loop under consideration, the twist portions of the loop occur at $\theta = 0, \pi$ while the $+1/2$ wedge portion occurs at $\theta = \pi/2$ and the $-1/2$ wedge portion occurs at $\theta = 3\pi/2$ (figure 10). For $L_2 > 0$, equation (5.18) shows significant asymmetry in the evolution of the loop. The fastest sections of the loop turn out to be the twist sections, which is the opposite result to that obtained for straight, parallel line disclinations. For $L_2 > 0$, the bend and splay constants increase while the twist constant remains the same, and hence straight wedge ($\hat{\boldsymbol{\Omega}} \cdot \hat{\mathbf{T}} = \pm 1$) disclinations will annihilate faster (because they cost more elastic energy) than straight twist ($\hat{\boldsymbol{\Omega}} \cdot \hat{\mathbf{T}} = 0$) disclinations. Therefore it is the coupling to disclination curvature that causes this asymmetry.

Additionally, there is asymmetry predicted in the wedge sections due to the $\sin\theta$ term in equation (5.18). This predicts that the $-1/2$ wedge section moves faster than the $+1/2$ wedge section if $L_2 > 0$. This is also against our intuition since the splay and bend constants are still equal for this set of parameters, and so for straight, parallel lines these two wedge defects would still annihilate symmetrically. We also note that equation (5.18) holds regardless of the choice of $\hat{\mathbf{n}}_0$ in the yz plane.

We examine the predictions of equation (5.18) through computation with the full $\mathbf{Q}$-tensor equations. For this computation, all parameters are the same as previous computations, except we now set $L_2 = 2$ which corresponds to a ratio of splay (or bend) to twist $K_{11}/K_{22} = 2$. Figure 11 shows the predicted velocity alongside several time slices of the computational results. The predicted velocity very accurately captures the evolution of the loop, particularly at early times when the loop is circular. In the computation, the twist sections of the loop disclination move fastest and there is asymmetry between the $+1/2$ and $-1/2$ wedge sections. We note that recent experiments on systems of line and loop disclinations have not reported this asymmetry in loop annihilation, even though the experimental system has a twist constant approximately half that of the splay and bend constants [73]. This may indicate that all observed loop disclinations were

Downloaded from https://royalsocietypublishing.org/ on 06 November 2023

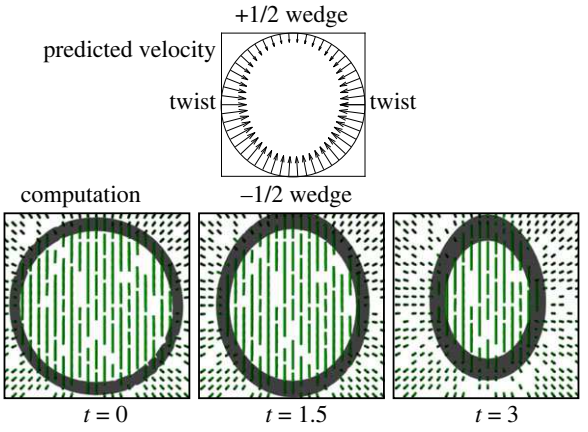

Figure 11. Annihilation of an initially circular wedge-twist loop disclination with $L_2 > 0$. The top panel shows the predicted velocity calculated in equation (5.18). The bottom panels show the configuration in the computation at three different times. The cylinders represent the nematic director, while the contours depict the extent of the disclination loop where $S = 0.3S_N$.

twist type. This suggests that analytical calculations using the kinematic velocity law may be used to classify disclination types in experimental systems in which the material parameters are known.

(e) Defect sorting with external fields and flows

The final application of the kinematic law we examine is the motion of disclination lines under external fields or applied flows. These are two common situations studied in experiments on nematics, and are important in technological and biological applications as well as in the context of active nematics [12,31,74–82].

(i) External fields

We first consider an external field that couples to the tensor order parameter free energy as $f_H = -\chi \mathbf{H}^T\mathbf{Q}\mathbf{H}$ where $\mathbf{H}$, the external field, can be an electric or magnetic field [29], and χ is the susceptibility. If $\chi > 0$ this energy is minimized when $(\hat{\mathbf{n}} \cdot \mathbf{H})^2 = |\mathbf{H}|^2$, that is, when the director aligns or anti-aligns with the field. For our purposes, the contribution to the time dependence of $\mathbf{Q}$ arising from this coupling is

$$\partial_t Q_{ij} = \chi H_i H_j. \tag{5.19}$$

The resulting velocity of a single, straight line disclination with constant $\hat{\boldsymbol{\Omega}}$, assuming that the line lies along the z-axis and that it is oriented so $\phi_0 = 0$ corresponds to the positive x-axis, is

$$\mathbf{v} = \frac{\chi |\mathbf{H}|^2 a}{S_N}[((\hat{\mathbf{H}} \cdot \hat{\mathbf{n}}_0)^2 - (\hat{\mathbf{H}} \cdot \hat{\mathbf{n}}_1)^2)\hat{\mathbf{x}} + 2(\hat{\mathbf{H}} \cdot \hat{\mathbf{n}}_0)(\hat{\mathbf{H}} \cdot \hat{\mathbf{n}}_1)\hat{\mathbf{y}}] \tag{5.20}$$

where $\hat{\mathbf{H}}$ is the unit vector in the direction of the applied field. If $\mathbf{H}$ is in the direction of $\hat{\boldsymbol{\Omega}}$, equation (5.20) shows there will be no motion of the disclination. Thus, we may limit further analysis to two dimensions and we will set $\hat{\boldsymbol{\Omega}} = \pm\hat{\mathbf{z}}$ and $\hat{\mathbf{n}}_0 = \hat{\mathbf{x}}$. Note that if $\hat{\boldsymbol{\Omega}} \neq \hat{\mathbf{z}}$ then the following analysis holds for $\mathbf{H}$ in the plane perpendicular to $\hat{\boldsymbol{\Omega}}$. If we let $\hat{\mathbf{H}} = (\cos\beta, \sin\beta, 0)$, equation (5.20) reduces to

$$\mathbf{v} = -\frac{\chi |\mathbf{H}|^2 a}{S_N}[\cos 2\beta\hat{\mathbf{x}} + 2m \sin 2\beta\hat{\mathbf{y}}], \tag{5.21}$$

where $m = \pm 1/2$ is the charge of the effective two-dimensional disclination.

Downloaded from https://royalsocietypublishing.org/ on 06 November 2023

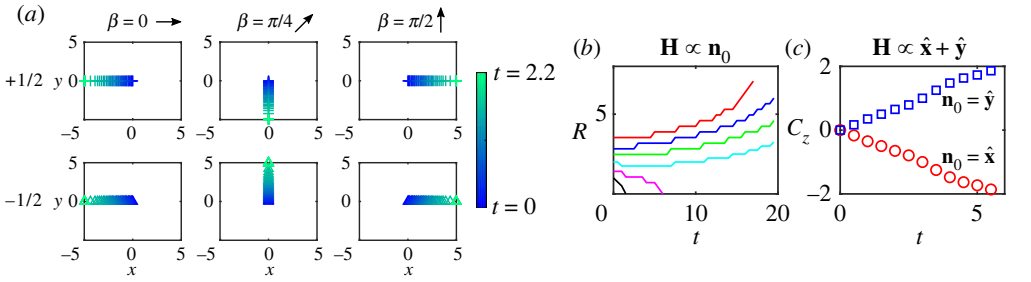

Figure 12. (*a*) Disclination motion in the presence of an external field $\mathbf{H} = |\mathbf{H}|(\cos\beta, \sin\beta)$. The top panels show the trajectories of $+1/2$ wedge disclinations while the bottom panels show the trajectories of $-1/2$ wedge disclinations. The colour indicates the time (in computational units). (*b–c*) Computed motion of twist disclination loops ($\hat{\boldsymbol{\Omega}} = \hat{\mathbf{z}}$) in the presence of an external field $\mathbf{H}$. (*b*) Loop radius R versus time t for various initial radii when $\mathbf{H}$ is in the direction $\hat{\mathbf{n}}_0$. Above an initial radius $R_0 \approx 2$, the loop grows indefinitely instead of self-annihilating. (*c*) z-coordinate of the centre of a twist disclination loop C_z versus t when $\mathbf{H} \propto \hat{\mathbf{x}} + \hat{\mathbf{y}}$. Two cases are shown: when $\hat{\mathbf{n}}_0 = \hat{\mathbf{x}}$ the loop moves in the $-\hat{\mathbf{z}}$ direction while the opposite occurs when $\hat{\mathbf{n}}_0 = \hat{\mathbf{y}}$.

Equation (5.21) shows that if the field is aligned or anti-aligned with $\hat{\mathbf{x}}$ the disclination will move in the $-\hat{\mathbf{x}}$ direction. On the other hand, if the field is aligned or anti-aligned with $\hat{\mathbf{y}}$ the disclination will move in the $+\hat{\mathbf{x}}$ direction. This behaviour is predicted to be independent of the charge of the disclination. However, if $\hat{\mathbf{H}}$ is skewed from these two alignments there is a predicted component of the velocity along the $\pm\hat{\mathbf{y}}$ direction, which depends on the charge m. Thus for disclinations that are oriented in the same direction, a skewed field will deflect oppositely charged disclinations in opposite directions.

We demonstrate this behaviour by computing time-dependent configurations in a two-dimensional nematic with in plane field $\mathbf{H}$. For the computations, we set $\Delta t = 0.5$, $\chi = 1$ and $|\mathbf{H}| = 0.5$. In figure 12*a*, we show trajectories for $\pm 1/2$ disclinations with $\hat{\mathbf{n}}_0 = \hat{\mathbf{x}}$ and $\beta = 0, \pi/4, \pi/2$. As shown in the figure, we find that equation (5.21) correctly predicts the direction of motion for the disclinations. In particular, when $\beta = \pi/4$ the motion of the $\pm 1/2$ disclinations is opposite one another, and hence the effect of this applied skewed field is to sort the disclinations by topological charge.

We may also compute the effect of external fields on three-dimensional disclination loops. Applying the kinematic equation as we did in the previous section, assuming $L_2 = 0$, we find

$$\mathbf{v} = \frac{\chi |\mathbf{H}|^2 a}{S_N}[((\hat{\mathbf{H}} \cdot \hat{\mathbf{n}}_0)^2 - (\hat{\mathbf{H}} \cdot \hat{\mathbf{n}}_1)^2)\hat{\boldsymbol{\rho}} - 2(\hat{\mathbf{H}} \cdot \hat{\mathbf{n}}_0)(\hat{\mathbf{H}} \cdot \hat{\mathbf{n}}_1)\hat{\mathbf{z}}] - \frac{3}{2R}\hat{\boldsymbol{\rho}} \tag{5.22}$$

where the second term is the self-annihilation term derived above in equation (5.16). Equation (5.22) predicts a multitude of differing trajectories depending on $\hat{\boldsymbol{\Omega}}$ and $\hat{\mathbf{n}}_0$. For the case of $\hat{\boldsymbol{\Omega}} = \hat{\mathbf{z}}$, a pure twist loop, only field components in the plane of the disclination loop are predicted to affect it. In this case, interestingly, if the field is directed along $\hat{\mathbf{n}}_0$ equation (5.22) predicts an unstable equilibrium radius of the loop. If the radius is smaller than the unstable length, the loop will self-annihilate. However, if the radius is larger than this length, the field will induce a continued growth in the loop. Additionally, if the field is skewed between the directions $\hat{\mathbf{n}}_0$ and $\hat{\mathbf{n}}_1$, equation (5.22) predicts the disclination loop will deflect along the $\hat{\mathbf{z}}$ direction, depending on $\hat{\mathbf{n}}_0$ and $\hat{\mathbf{n}}_1$, that is, depending on the geometric properties of the loop.

We have also tested this prediction by solving the full $\mathbf{Q}$-tensor equations with $\mathbf{H} = 0.65\hat{\mathbf{n}}_0$ ($\hat{\mathbf{n}}_0 = \hat{\mathbf{x}}$) and the rest of the parameters the same as above, only now in three dimensions for a pure twist loop. Figure 12*b* shows the computed radius as a function of time for various initial radii. At $R_C \approx 2$, we find the loop changes behaviour from shrinking to growing indefinitely as predicted by equation (5.22). From the computations, we estimate $a \approx 0.75$, which leads to a predicted critical radius from equation (5.22) of $R_C \approx 2.1$, very close to our computational result.

Downloaded from https://royalsocietypublishing.org/ on 06 November 2023

Additionally, figure 12*c* shows the z-coordinate of the centre of a loop C_z as a function of time for cases in which $\mathbf{H} \propto \hat{\mathbf{x}} + \hat{\mathbf{y}}$ with $\hat{\mathbf{n}}_0 = \hat{\mathbf{x}}$ and $\hat{\mathbf{n}}_0 = \hat{\mathbf{y}}$. As evidenced by the figure, the loop coherently moves down (up) along the z-axis when $\hat{\mathbf{n}}_0 = \hat{\mathbf{x}}$ ($\hat{\mathbf{n}}_0 = \hat{\mathbf{y}}$), as predicted by equation (5.22).

External fields have been shown to effectively identify disclinations either by topological or geometric content. Thus, these simple analytical results may lead to a number of applications in which different types of disclinations correspond to different active nematic or biological motifs. Colloidal particles, or differing cell types, have been shown to preferentially accumulate at regions of differing topological or geometric character, and hence external fields may allow particle and cell sorting [10,32,83–85]. We note that the velocities given here (particularly the two dimensional equation (5.21)) could have also been predicted from the energy directly, since the effect of the field is to align the director. However, having the analytical tool is useful for more complex scenarios where energy methods may not be analytically viable.

(ii) Shear flow

The motion of a disclination in an imposed flow $\mathbf{u}$ is studied next. We assume the time dependence of $\mathbf{Q}$ is given by the Beris-Edwards model [30]:

$$\partial_t \mathbf{Q} = -(\mathbf{u}\cdot\nabla)\mathbf{Q} + \lambda\left[\mathbf{E}\mathbf{Q} + \mathbf{Q}\mathbf{E} + \frac{2}{3}\mathbf{E} - 2\left(\mathbf{Q} + \frac{1}{3}\right)(\mathbf{Q}:\nabla\mathbf{u})\right] + [\mathbf{W},\mathbf{Q}] - \left[\frac{\delta F}{\delta \mathbf{Q}}\right]^{TS}, \tag{5.23}$$

where $2\mathbf{E} = \nabla\mathbf{u} + \nabla\mathbf{u}^T$ is the strain rate tensor, $2\mathbf{W} = \nabla\mathbf{u} - \nabla\mathbf{u}^T$ is the vorticity tensor, λ is the 'tumbling' parameter related to the tendency for the nematogens to align with shear [86,87], and $[\cdot,\cdot]$ is the commutator of two tensors. We choose this model because it is commonly employed in computational studies of active nematics in which disclinations play a primary role [88].

First, consider the contribution of the first term on the right-hand side of equation (5.23). This is the traditional advection term and is the only non-zero term in the case of uniform flow. The kinematic velocity equation for disclinations gives, for any segment of disclination with tangent vector $\hat{\mathbf{T}}$,

$$\mathbf{v} = 2\hat{\mathbf{T}} \times (\mathbf{u} \times \hat{\mathbf{T}}) + \text{relaxation}, \tag{5.24}$$

where '+ relaxation' stands for terms already discussed attributed to the diffusive relaxation of the disclination (for the rest of this section we will omit these terms though it is understood they still contribute to disclination motion). The right hand side of equation (5.24) may also be written as $2[\mathbf{u} - (\mathbf{u}\cdot\hat{\mathbf{T}})\hat{\mathbf{T}}]$, indicating that the flow in this case simply advects the disclination in the direction perpendicular to $\hat{\mathbf{T}}$, with the speed reduced by the amount that $\hat{\mathbf{T}}$ and $\mathbf{u}$ overlap. This is the expected result, and has been shown for two-dimensional disclinations already [44].

To study the effect of a more complicated—yet highly relevant—imposed flow, we turn our attention to an imposed shear flow,

$$\mathbf{u}(\mathbf{r}) = \gamma(\mathbf{r}\cdot\hat{\mathbf{w}})\hat{\mathbf{u}}, \tag{5.25}$$

where γ is the shear rate, $\hat{\mathbf{u}}$ is the direction of the flow, and $\hat{\mathbf{w}}\cdot\hat{\mathbf{u}} = 0$. In this case, the tensors $\mathbf{E}$ and $\mathbf{W}$ are non-zero. However, because we only need to compute $\partial_t\mathbf{Q}$ at the disclination core to apply equation (3.6), it is easy to show that all terms in equation (5.23) that multiply $\mathbf{Q}$ will give zero in the computation of the disclination velocity. This is analogous to the case presented in §4 in which terms involving $\mathbf{Q}^n$ for some power n do not contribute to the disclination velocity. Thus, the only term we must consider is the flow aligning term, $(2\lambda/3)\mathbf{E}$. For the shear flow given,

$$\mathbf{E} = \frac{\gamma}{2}(\hat{\mathbf{w}}\otimes\hat{\mathbf{u}} + \hat{\mathbf{u}}\otimes\hat{\mathbf{w}}). \tag{5.26}$$

Downloaded from https://royalsocietypublishing.org/ on 06 November 2023

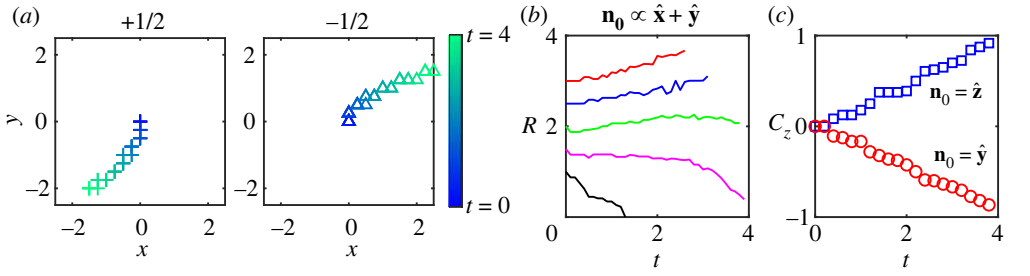

Figure 13. (*a*) Trajectories of ±1/2 wedge disclinations in the presence of the shear flow $\mathbf{u} = \gamma y\hat{\mathbf{x}}$ for $\gamma = 2$. As predicted in equation (5.28), ± 1/2 disclinations move in opposite directions depending on their charge. The colour indicates the time (in computational units). (*b-c*) Motion of wedge-twist disclination loops ($\hat{\boldsymbol{\Omega}} = \hat{\mathbf{x}}$) in shear flow $\mathbf{u} = \gamma z\hat{\mathbf{y}}$ for $\gamma = 2$. (*b*) Loop radius R versus time t for various initial radii with $\hat{\mathbf{n}}_0 \propto \hat{\mathbf{x}} + \hat{\mathbf{y}}$. The radius of the loop is calculated by finding the average distance between the centre of the loop and points in which $S < 0.3S_N$. Above $R \approx 2$ the loop disclinations grow indefinitely. (*c*) z coordinate of the centre of the loop, C_z, versus t for the cases $\hat{\mathbf{n}}_0 = \hat{\mathbf{z}}$ and $\hat{\mathbf{n}}_0 = \hat{\mathbf{y}}$. For these cases, depending on $\hat{\mathbf{n}}_0$, the loop has a positive or negative velocity component in the $\hat{\mathbf{z}}$ direction.

For a straight line disclination with constant $\hat{\boldsymbol{\Omega}}$ and $\hat{\mathbf{T}} = \hat{\mathbf{z}}$, the flow contribution to the line velocity is

$$\mathbf{v} = 2\hat{\mathbf{z}} \times (\mathbf{u} \times \hat{\mathbf{z}}) + \frac{2\lambda\gamma a}{3S_N}\Big[\Big((\hat{\mathbf{w}} \cdot \hat{\mathbf{n}}_1)(\hat{\mathbf{u}} \cdot \hat{\mathbf{n}}_1) - (\hat{\mathbf{w}} \cdot \hat{\mathbf{n}}_0)(\hat{\mathbf{u}} \cdot \hat{\mathbf{n}}_0)\Big)\hat{\mathbf{x}} - \Big((\hat{\mathbf{w}} \cdot \hat{\mathbf{n}}_0)(\hat{\mathbf{u}} \cdot \hat{\mathbf{n}}_1) + (\hat{\mathbf{w}} \cdot \hat{\mathbf{n}}_1)(\hat{\mathbf{u}} \cdot \hat{\mathbf{n}}_0)\Big)\hat{\mathbf{y}}\Big]. \tag{5.27}$$

Equation (5.27) is similar to the velocity resulting from an imposed field, equation (5.20), except there are two important directions instead of one. In particular, equation (5.27) predicts that if either the flow direction, $\hat{\mathbf{u}}$, or the shear direction, $\hat{\mathbf{w}}$, are parallel to $\hat{\boldsymbol{\Omega}}$, the only contribution to the disclination velocity from the flow will be advection.

An illustrative example is when $\hat{\boldsymbol{\Omega}} = \pm\hat{\mathbf{z}}$, $\hat{\mathbf{n}}_0 = \hat{\mathbf{x}}$, $\hat{\mathbf{u}} = \hat{\mathbf{x}}$, and $\hat{\mathbf{w}} = \hat{\mathbf{y}}$. This is the effective two-dimensional case for ±1/2 disclinations. For this configuration, equation (5.27) reduces to

$$\mathbf{v} = 2\gamma y\hat{\mathbf{x}} - 2m\frac{4\lambda\gamma a}{3S_N}\hat{\mathbf{y}}, \tag{5.28}$$

where $m = \pm 1/2$ is the topological charge of the disclination. The first term in equation (5.28) is advection by the flow field, while the second arises from the tendency for the nematogens to flow align in shear flows. Just as with the applied field, the motion in the $\hat{\mathbf{y}}$ direction changes depending on the topological charge of the disclination m, assuming disclinations are oriented identically. We note that this result was also predicted for a purely two-dimensional liquid crystal in reference [44].

To test this result, the full Beris-Edwards equations, equation (5.23), for a nematic are solved under an imposed shear flow $\mathbf{u} = \gamma y\hat{\mathbf{x}}$. We compute the effect of flow on ±1/2 disclinations initially located at the origin. For the computation we set $\Delta t = 0.1$, $\lambda = 1$, and $\gamma = 2$. Figure 13*a* shows the trajectories of the disclinations over time. The disclinations have a component of their velocity along either the $\pm\hat{\mathbf{y}}$ directions depending on their charge, which is predicted by equation (5.28). Much like the case of the applied field, these results demonstrate that an applied shear flow may be used as a sorting agent for disclinations of opposite charge, while the full behaviour, equation (5.27) may be used to predict the motion of disclinations in the more general scenario.

Note that there is an asymmetry between the trajectories of the +1/2 and −1/2 disclinations in figure 13*a*. This can be understood as a higher order effect resulting from the change in director near the core. From the Beris-Edwards equations, equation (5.23), the rate of change of the director

Downloaded from https://royalsocietypublishing.org/ on 06 November 2023

will be dependent on S (and P). Thus, since $\nabla S \neq 0$ at the core, there will be, over time, a non-zero $\nabla\tilde{\varphi}$. This will then lead to additional motion of the disclination as per the discussion of §4. Because this effect is due to the relaxational terms of the dynamics, we expect that if $\gamma \gg 1/\tau$ (that is, the shear flow is much faster than the relaxation rate of the nematic) this effect will be negligible. This is likely the case in experiments involving shear flow [81]. In our numerics, however, we have set $\gamma \sim 1/\tau$ due to computational limitations.

Finally, it is possible to obtain the evolution under shear flow of a disclination loop in a similar manner to the prediction of the external field. Assuming the loop lies in the xy plane, we find

$$\mathbf{v} = 2\hat{\boldsymbol{\theta}} \times (\mathbf{u} \times \hat{\boldsymbol{\theta}}) - \frac{3}{2R}\hat{\boldsymbol{\rho}} + \frac{2\lambda\gamma a}{3S_N}\Big[\Big((\hat{\mathbf{w}}\cdot\hat{\mathbf{n}}_0)(\hat{\mathbf{u}}\cdot\hat{\mathbf{n}}_0) - (\hat{\mathbf{w}}\cdot\hat{\mathbf{n}}_1)(\hat{\mathbf{u}}\cdot\hat{\mathbf{n}}_1)\Big)\hat{\boldsymbol{\rho}} - \Big((\hat{\mathbf{w}}\cdot\hat{\mathbf{n}}_0)(\hat{\mathbf{u}}\cdot\hat{\mathbf{n}}_1) + (\hat{\mathbf{w}}\cdot\hat{\mathbf{n}}_1)(\hat{\mathbf{u}}\cdot\hat{\mathbf{n}}_0)\Big)\hat{\mathbf{z}}\Big], \tag{5.29}$$

where we have included the self-annihilation term predicted in equation (5.16). Equation (5.29) is similar to equation (5.27), except the tangent vector is $\hat{\mathbf{T}} = \hat{\boldsymbol{\theta}}$ and the directions of motion are $\hat{\boldsymbol{\rho}}$ and $\hat{\mathbf{z}}$ as in equation (5.22). Equation (5.29) predicts many similar features to that of the applied field, except for the addition of advection. For instance, fixing the shear flow directions to $\hat{\mathbf{w}} = \hat{\mathbf{z}}$ and $\hat{\mathbf{u}} = \hat{\mathbf{y}}$ and setting $\hat{\boldsymbol{\Omega}} = \hat{\mathbf{x}}$ gives similar results to the applied field, and the motion is dependent on the angle between $\hat{\mathbf{n}}_0$ and the z-axis. If $\hat{\mathbf{n}}_0 = \hat{\mathbf{z}}$, the loop is predicted to have a component of the velocity in the $+\hat{\mathbf{z}}$ direction. On the other hand, if $\hat{\mathbf{n}}_0 = \hat{\mathbf{y}}$ the loop is predicted to move oppositely. If $\hat{\mathbf{n}}_0$ is skewed from these two directions, there will be an additional velocity in the $\hat{\boldsymbol{\rho}}$ direction. Particularly, if $\hat{\mathbf{n}}_0 \propto \hat{\mathbf{y}} + \hat{\mathbf{z}}$, there will be an unstable critical radius above which the loop will continue to grow. We note that growing disclination loops above a critical radius have been observed experimentally and predicted theoretically for the case of Poiseuille flow through a small channel [89,90].

We have numerically tested these predictions for the cases outlined above for a full three-dimensional disclination loop under shear flow. We perform the same analysis as with the applied field: figure 13*b* shows the radius of the loop as a function of time for various initial radii when $\hat{\mathbf{n}}_0 = (1/\sqrt{2})(\hat{\mathbf{y}} + \hat{\mathbf{z}})$, and figure 13*c* shows the z-component of the centre of the loop disclination, C_z, for the cases $\hat{\mathbf{n}}_0 = \hat{\mathbf{z}}$ and $\hat{\mathbf{n}}_0 = \hat{\mathbf{y}}$. For the computations, we use the same parameters as indicated above. We see from the figures that the motion of the disclination loops are qualitatively well described by equation (5.29).

That coupling to shear flow yields similar disclination motion to that of an applied field is a striking, yet intuitive result. For a flow aligning nematic, there is a steady state in which the director everywhere is given by some angle to the flow [87,91]. Thus, shear flow has a similar effect on a uniform nematic to an applied field and so it is not surprising that it would have similar effects on disclinations. However, theoretically (and in particular analytically) proving that the effects are similar on disclinations is not simple due to the nonlinear nature of the equations, and the fact that the system is out of equilibrium. This demonstrates the power of the kinematic description of disclinations, which allows analytical calculation even in non-equilibrium systems.

6. Discussion

We have derived a kinematic equation in terms of the nematic tensor order parameter at a disclination core that gives the velocity of three-dimensional disclination lines in nematic liquid crystals. In particular, we have generalized previous results involving order parameter singularity tracking methods to a case in which the order parameter is not singular at the defect core. The focus, instead, are zeros in a subspace of the order parameter space. Further, we have made use of the property that this velocity only depends on derivatives of the order parameter at the core to outline an approximation scheme that allows for analytic predictions of the disclination velocity in a number of cases of interest.

Downloaded from https://royalsocietypublishing.org/ on 06 November 2023

The geometric complexity of three-dimensional disclination lines has proven a barrier in the study of even the simplest configurations containing multiple disclinations. Here we have presented analytic results which either reinterpret previous results or yield novel predictions for disclination motion. They include equations for the motion of twisted disclinations in two dimensions, recombining and rotating disclination lines in three dimensions, self-annihilating disclination loops with both isotropic and anisotropic elasticity, and disclination lines and loops under externally applied fields and flows. All of these configurations are of current interest and importance in studies of the coarsening and control of passive and active nematics.

The results and methods presented in this work should be of considerable use to experimental and large-scale simulation studies in which disclinations play important roles. As demonstrated in §5e, applying fields or flows to systems of disclinations allows the identification of disclination geometry and topology without the explicit recreation of the order parameter. Additionally, the methods may be used to engineer disclination motion which can be further used as particle aggregators and transporters.

One aspect of disclination evolution that still needs resolution is the evolution of the rotation vector. Because it is not topologically protected, the rotation vector may change as a function of time. This behaviour is different from the seemingly similar [26,92] Burgers vector characterizing dislocations in solids, which remains constant. A detailed study of how this geometric property evolves in time for various configurations will be important as it is intricately connected to the dynamics of disclination lines. Additionally, while we studied circular loops here with constant $\hat{\boldsymbol{\Omega}}$, disclinations in experiments are not perfectly circular and have rotation vectors that vary throughout the loop. Thus, a more general treatment of curvature and torsion of disclination lines as well as varying $\hat{\boldsymbol{\Omega}}$ may lead to a better understanding of their overall dynamics.

Another interesting area that we have not studied here is active nematics. These systems have been heavily studied in two dimensions [12,13,44,93,94] and three-dimensional active nematics are recently receiving more attention [14,24,27]. In active nematics, disclinations play a crucial role by driving flows into a mesoscopic chaotic state. Thus, understanding the behaviour of disclinations is highly important in this field. However, due to the chaotic nature of the flows, and the complex interaction with the geometric properties of disclinations, very little has been studied analytically regarding systems of many flowing disclinations. The kinematic equation presented here may prove to be a useful tool in understanding individual disclination dynamics in these out of equilibrium systems.

Finally, while we have focused here on the nematic phase, the methods presented in §§3 and 4 can be generalized to other systems with broken symmetries that support topological defects. The derivation of kinematic equations similar to equation (3.6) may yield fruitful analogies between otherwise physically dissimilar systems. For example, an equivalent to equation (3.6) was recently derived for dislocations in solids using a phase field approach [43]. Topological defects are also important in high energy physics and cosmology [17,95]. Comparison of kinematic velocities in these fields to condensed matter systems might allow for more cross disciplinary experiments.

Data accessibility. Matlab code for numerical calculations included as supplemental material.

The data are provided in electronic supplementary material [96].

Authors' contributions. C.D.S.: conceptualization, formal analysis, methodology, software, writing—original draft; J.V.: conceptualization, supervision, validation, writing—review and editing.

All authors gave final approval for publication and agreed to be held accountable for the work performed therein.

Conflict of interest declaration. We declare we have no competing interests.

Funding. This research has been supported by the National Science Foundation under grant no. DMR-1838977, and by the Minnesota Supercomputing Institute. C.D.S. also gratefully acknowledges support from the U.S. Department of Energy through the LANL/LDRD Program and the Center for Nonlinear Studies for part of this work.

Downloaded from https://royalsocietypublishing.org/ on 06 November 2023

Acknowledgements. We are indebted to Jonathan Selinger and Daniel Beller for many useful comments about this work.

References

1. Abrikosov A. 1957 The magnetic properties of superconducting alloys. *J. Phys. Chem. Solids* **2**, 199–208. (doi:10.1016/0022-3697(57)90083-5)
2. Chaikin PM, Lubensky TC. 1995 *Principles of condensed matter physics*. Cambridge, UK: Cambridge University Press.
3. Halperin BI, Nelson DR. 1978 Theory of two-dimensional melting. *Phys. Rev. Lett.* **41**, 121–124. (doi:10.1103/PhysRevLett.41.121)
4. Nelson DR, Halperin BI. 1979 Dislocation-mediated melting in two dimensions. *Phys. Rev. B* **19**, 2457–2484. (doi:10.1103/PhysRevB.19.2457)
5. Young AP. 1979 Melting and the vector Coulomb gas in two dimensions. *Phys. Rev. B* **19**, 1855–1866. (doi:10.1103/PhysRevB.19.1855)
6. Kleman M, Friedel J. 2008 Disclinations, dislocations, and continuous defects: a reappraisal. *Rev. Mod. Phys.* **80**, 61–115. (doi:10.1103/RevModPhys.80.61)
7. Etournay R, Merkel M, Popović M, Brandl H, Dye NA, Aigouy B, Salbreux G, Eaton S, Jülicher F. 2016 TissueMiner: a multiscale analysis toolkit to quantify how cellular processes create tissue dynamics. *eLife* **5**, e14334 (doi:10.7554/eLife.14334)
8. Livshits A, Shani-Zerbib L, Maroudas-Sacks Y, Braun E, Keren K. 2017 Structural inheritance of the actin cytoskeletal organization determines the body axis in regenerating hydra. *Cell Reports* **18**, 1410–1421. (doi:10.1016/j.celrep.2017.01.036)
9. Hoffmann LA, Carenza LN, Eckert J, Giomi L. 2022 Theory of defect-mediated morphogenesis. *Sci. Adv.* **8**, eabk2712 (doi:10.1126/sciadv.abk2712)
10. Ravnik M, Škarabot M, Žumer S, Tkalec U, Poberaj I, Babic D, Osterman N, Muševic I. 2007 Entangled nematic colloidal dimers and wires. *Phys. Rev. Lett.* **99**, 247801 (doi:10.1103/PhysRevLett.99.247801)
11. Čopar S, Žumer S. 2011 Nematic braids: topological invariants and rewiring of disclinations. *Phys. Rev. Lett.* **106**, 177801 (doi:10.1103/PhysRevLett.106.177801)
12. Doostmohammadi A, Ignés-Mullol J, Yeomans JM, Sagués F. 2018 Active Nematics. *Nat. Commun.* **9**, 3246. (doi:10.1038/s41467-018-05666-8)
13. Opathalage A, Norton MM, Juniper MPN, Langeslay B, Aghvami SA, Fraden S, Dogic Z. 2019 Self-organized dynamics and the transition to turbulence of confined active nematics. *Proc. Natl Acad. Sci. USA* **116**, 4788–4797. (doi:10.1073/pnas.1816733116)
14. Duclos G *et al.* 2020 Topological structure and dynamics of three-dimensional active nematics. *Science* **367**, 112–1124. (doi:10.1126/science.aaz4547)
15. Peach M, Koehler JS. 1950 The forces exerted on dislocations and the stress fields produced by them. *Phys. Rev.* **80**, 436–439. (doi:10.1103/PhysRev.80.436)
16. Blatter G, Feigel'man MV, Geshkenbein VB, Larkin AI, Vinokur VM. 1994 Vortices in high-temperature superconductors. *Rev. Mod. Phys.* **66**, 1125–1388. (doi:10.1103/RevModPhys.66.1125)
17. Pismen LM. 1999 *Vortices in nonlinear fields*. Oxford, UK: Oxford University Press.
18. Olson CJ, Reichhardt C, Jankó B, Nori F. 2001 Collective interaction-driven ratchet for transporting flux quanta. *Phys. Rev. Lett.* **87**, 177002 (doi:10.1103/PhysRevLett.87.177002)
19. Svenšek D, Žumer S. 2002 Hydrodynamics of pair-annihilating disclination lines in nematic liquid crystals. *Phys. Rev. E* **66**, 021712.
20. Kremen A, Wissberg S, Haham N, Persky E, Frenkel Y, Kalisky B. 2016 Mechanical control of individual superconducting vortices. *Nano Lett.* **16**, 1626–1630. (doi:10.1021/acs.nanolett.5b04444)
21. Tang X, Selinger JV. 2017 Orientation of topological defects in 2D nematic liquid crystals. *Soft Matter* **13**, 5481. (doi:10.1039/C7SM01195D)
22. Skaugen A, Angheluta L, Viñals J. 2018 Dislocation dynamics and crystal plasticity in the phase-field crystal model. *Phys. Rev. B* **97**, 054113. (doi:10.1103/PhysRevB.97.054113)
23. Acharya A, Viñals J. 2020 Field dislocation mechanics and phase field crystal models. *Phys. Rev. B* **102**, 064109 (doi:10.1103/PhysRevB.102.064109)
24. Binysh J, Kos Ž, Čopar S, Ravnik M, Alexander GP. 2020 Three-dimensional active defect loops. *Phys. Rev. Lett.* **124**, 088001. (doi:10.1103/PhysRevLett.124.088001)

Downloaded from https://royalsocietypublishing.org/ on 06 November 2023

25. Beliaev M, Zöllner D, Pacureanu A, Zaslansky P, Zlotnikov I. 2021 Dynamics of topological defects and structural synchronization in a forming periodic tissue. *Nat. Phys.* **17**, 410–415. (doi:10.1038/s41567-020-01069-z)
26. Long C, Tang X, Selinger RL, Selinger JV. 2021 Geometry and mechanics of disclination lines in 3D nematic liquid crystals. *Soft Matter* **17**, 2265. (doi:10.1039/D0SM01899F)
27. Houston AJ. 2021 Defect loops in three-dimensional active nematics as active multipoles. (http://arxiv.org/abs/2106.15424[cond-mat.soft])
28. Alexander GP, Chen BG, Matsumoto E, Kamien RD. 2012 Colloquium: disclination loops, point defects, and all that in nematic liquid crystals. *Rev. Mod. Phys.* **84**, 497. (doi:10.1103/RevModPhys.84.497)
29. de Gennes PG. 1975 *The physics of liquid crystals*. Oxford, UK: Oxford University Press.
30. Beris AN, Edwards BJ. 1994 *Thermodynamics of flowing systems*. Oxford, UK: Oxford University Press.
31. Yeh P, Gu C. 2009 *Optics of liquid crystal displays*. New York (Chichester, UK): Wiley.
32. Gu Y, Abbott NL. 2000 Observation of saturn-ring defects around solid microspheres in nematic liquid crystals. *Phys. Rev. Lett.* **85**, 4719. (doi:10.1103/PhysRevLett.85.4719)
33. Peng C, Guo Y, Conklin C, Viñals J, Shiyanovskii SV, Wei QH, Lavrentovich OD. 2015 Liquid crystals with patterned molecular orientation as an electrolytic active medium. *Phys. Rev. E* **92**, 052502. (doi:10.1103/PhysRevE.92.052502)
34. Babakhanova G, Turiv T, Guo Y, Hendrikx M, Wei QH, Schenning AP, Broer DJ, Lavrentovich OD. 2018 Liquid crystal elastomer coatings with programmed response of surface profile. *Nat. Commun.* **9**, 456. (doi:10.1038/s41467-018-02895-9)
35. Turiv T, Krieger J, Babakhanova G, Yu H, Shiyanovskii SV, Wei QH, Kim MH, Lavrentovich OD. 2020 Topology control of human fibroblast cells monolayer by liquid crystal elastomer. *Sci. Adv.* **6**, eaaz6485 (doi:10.1126/sciadv.aaz6485)
36. Guo Y, Jiang M, Afghah S, Peng C, Selinger RLB, Lavrentovich OD, Wei QH. 2021 Photopatterned designer disclination networks in nematic liquid crystals. *Adv. Optical Mater.* **9**, 2100181. (doi:10.1002/adom.202100181)
37. Doostmohammadi A, Shendruk TN, Thijssen K, Yeomans JM. 2016 Onset of meso-scale turbulence in active nematics. *Nat. Commun.* **8**, 15326. (doi:10.1038/ncomms15326)
38. Halperin BI. 1981 Statistical mechanics of topological defects. In *Physics of defects* (ed. R Balian), p. 813. Amsterdam, The Netherlands: North-Holland Pub. Co.
39. Liu F, Mazenko GF. 1992 Defect-defect correlation in the dynamics of first-order phase transitions. *Phys. Rev. B* **46**, 5963. (doi:10.1103/PhysRevB.46.5963)
40. Mazenko GF, Wickham RA. 1997 Ordering kinetics of defect structures. *Phys. Rev. E* **57**, 2539. (doi:10.1103/PhysRevE.57.2539)
41. Mazenko GF. 1999 Velocity distribution for strings in phase-ordering kinetics. *Phys. Rev. E* **59**, 1574. (doi:10.1103/PhysRevE.59.1574)
42. Skaugen A, Angheluta L, Viñals J. 2018 Separation of elastic and plastic timescales in a phase field crystal model. *Phys. Rev. Lett.* **121**, 255501. (doi:10.1103/PhysRevLett.121.255501)
43. Skogvoll V, Angheluta L, Skaugen A, Salvalaglio M, Viñals J. 2022 A phase field crystal theory of the kinematics of dislocation lines. *J. Mech. Phys. Solids* **166**, 104932. (doi:10.1016/j.jmps.2022.104932)
44. Angheluta L, Chen Z, Marchetti MC, Bowick MJ. 2021 The role of fluid flow in the dynamics of active nematic defects. *New J. Phys.* **23**, 033009. (doi:10.1088/1367-2630/abe8a8)
45. Friedel J, De Gennes P. 1969 Boucles de disclination dans les cristaux liquides. *CR Acad. Sc. Paris B* **268**, 257–259.
46. Schopohl N, Sluckin T. 1987 Defect core structure in nematic liquid crystals. *Phys. Rev. Lett.* **59**, 22. (doi:10.1103/PhysRevLett.59.2582)
47. Schimming CD, Viñals J. 2020 Computational molecular field theory for nematic liquid crystals. *Phys. Rev. E.* **101**, 032702. (doi:10.1103/PhysRevE.101.032702)
48. Schimming CD, Viñals J, Walker SW. 2021 Numerical method for the equilibrium configurations of a Maier-Saupe bulk potential in a Q-tensor model of an anisotropic nematic liquid crystal. *J. Comp. Phys.* **441**, 110441. (doi:10.1016/j.jcp.2021.110441)
49. Feynman R. 1955 Application of quantum mechanics to liquid helium, ch. II. In *Progress in low temperature physics* (ed. CJ Gorter), vol. 1, pp. 17–53. Amsterdam, The Netherlands: Elsevier.
50. Kim YK, Shiyanovskii SV, Lavrentovich OD. 2013 Morphogenesis of defects and tactoids during isotropic-nematic phase transition in self-assembled lyotropic chromonic liquid crystals. *J. Phys.: Condens. Matter* **25**, 404202. (doi:10.1088/0953-8984/25/40/404202)

Downloaded from https://royalsocietypublishing.org/ on 06 November 2023

51. Zhou S, Shiyanovskii SV, Park HS, Lavrentovich OD. 2017 Fine structure of the topological defect cores studied for disclinations in lyotropic chromonic liquid crystals. *Nat. Commun.* **8**, 14974. (doi:10.1038/ncomms14974)
52. Schimming CD, Viãls J. 2022 Singularity identification for the characterization of topology, geometry, and motion of nematic disclination lines. *Soft Matter* **18**, 2234–2244. (doi:10.1039/D1SM01584B)
53. Kléman M. 1983 *Points, lines, and walls*. New York, NY: Wiley.
54. Long C, Deutsch MJ, Angelo J, Culbreath C, Yokoyama H, Selinger JV, Selinger RLB. 2022 Frank-read mechanism in nematic liquid crystals. (doi:10.48550/arxiv.2212.01316)
55. Ball JM, Majumdar A. 2010 Nematic liquid crystals: from Maier-Saupe to a continuum theory. *Mol. Liq. Cryst.* **525**, 1. (doi:10.1080/15421401003795555)
56. Frank F. 1958 On the theory of liquid crystals. *Discuss. Faraday Soc.* **25**, 19. (doi:10.1039/df9582500019)
57. Longa L, Monselesan D, Trebin HR. 1987 An extension of the Landau-Ginzberg-de Gennes theory for liquid crystals. *Liq. Cryst.* **2**, 769. (doi:10.1080/02678298708086335)
58. Selinger JV. 2018 Interpretation of saddle-splay and the Oseen-Frank free energy in liquid crystals. *Liq. Cryst. Rev.* **6**, 129–142. (doi:10.1080/21680396.2019.1581103)
59. Wise SM, Wang C, Lowengrub JS. 2009 An energy-stable and convergent finite-difference scheme for the phase field crystal equation. *SIAM J. Numer. Anal.* **47**, 2269–2288. (doi:10.1137/080738143)
60. Zhao J, Wang Q. 2016 Semi-discrete energy-stable schemes for a tensor-based hydrodynamic model of nematic liquid crystal flows. *J. Sci. Comput.* **68**, 1241–1266. (doi:10.1007/s10915-016-0177-x)
61. Xu J, Li Y, Wu S, Bousquet A. 2019 On the stability and accuracy of partially and fully implicit schemes for phase field modeling. *Comput. Methods Appl. Mech. Eng.* **345**, 826–853. (doi:10.1016/j.cma.2018.09.017)
62. Walker SW. 2018 FELICITY: a Matlab/C++ toolbox for developing finite element methods and simulation modeling. *SIAM J. Sci. Comput.* **40**, C234–C257. (doi:10.1137/17M1128745)
63. Notay Y. 2010 An aggregation-based algebraic multigrid method. *Electron. Trans. Numer. Anal.* **37**, 123–146.
64. Napov A, Notay Y. 2011 Algebraic analysis of aggregation-based multigrid. *Numer. Linear Algebra Appl.* **18**, 539–564. (doi:10.1002/nla.741)
65. Napov A, Notay Y. 2012 An algebraic multigrid method with guaranteed convergence rate. *SIAM J. Sci. Comput.* **34**, A1079–A1109. (doi:10.1137/100818509)
66. Notay Y. 2012 Aggregation-based algebraic multigrid for convection-diffusion equations. *SIAM J. Sci. Comput.* **34**, A2288–A2316. (doi:10.1137/110835347)
67. Tóth G, Denniston C, Yeomans JM. 2002 Hydrodynamics of topological defects in nematic liquid crystals. *Phys. Rev. Lett.* **88**, 105504. (doi:10.1103/PhysRevLett.88.105504)
68. Vromans AJ, Giomi L. 2016 Orientational properties of nematic disclinations. *Soft Matter* **12**, 6490. (doi:10.1039/C6SM01146B)
69. Pearce DJG, Kruse K. 2021 Properties of twisted topological defects in 2D nematic liquid crystals. *Soft Matter* **17**, 7408. (doi:10.1039/D1SM00825K)
70. Hudson SD, Thomas EL. 1989 Frank elastic-constant anisotropy measured from transmission-electron-microscope images of disclinations. *Phys. Rev. Lett.* **62**, 1993. (doi:10.1103/PhysRevLett.62.1993)
71. Schimming CD, Viñals J. 2020 Anisotropic disclination cores in nematic liquid crystals modeled by a self-consistent molecular field theory. *Phys. Rev. E* **102**, 010701. (doi:10.1103/PhysRevE.102.010701)
72. Dzyaloshinsky IE. 1970 Theory of disinclinations in liquid crystals. *Sov. Phys. JETP* **31**, 773–780.
73. Zushi Y, Takeuchi KA. 2022 Scaling and spontaneous symmetry restoring of topological defect dynamics in liquid crystal. *Proc. Natl Acad. Sci. USA* **119**, e2207349119 (doi:10.1073/pnas.2207349119)
74. Cladis PE, van Saarloos W, Finn PL, Kortan AR. 1987 Dynamics of line defects in nematic liquid crystals. *Phys. Rev. Lett.* **58**, 222–225. (doi:10.1103/PhysRevLett.58.222)
75. Vella A, Intartaglia R, Blanc C, Smalyukh II, Lavrentovich OD, Nobili M. 2005 Electric-field-induced deformation dynamics of a single nematic disclination. *Phys. Rev. E* **71**, 061705. (doi:10.1103/PhysRevE.71.061705)
76. Biscari P, Sluckin TJ. 2005 Field-induced motion of nematic disclinations. *SIAM J. Appl. Math.* **65**, 2141–2157. (doi:10.1137/040618898)

Downloaded from https://royalsocietypublishing.org/ on 06 November 2023

77. Lazo I, Peng C, Xiang J, Shiyanovskii SV, Lavrentovich OD. 2014 Liquid crystal-enabled electroosmosis through spatial charge separation in distorted regions as a novel mechanism of electrokinetics. *Nat. Commun.* **5**, 5033. (doi:10.1038/ncomms6033)
78. Wang M, He L, Zorba S, Yin Y. 2014 Magnetically actuated liquid crystals. *Nano Lett.* **14**, 3966–3971. (doi:10.1021/nl501302s)
79. Peng C, Guo Y, Conklin C, Viñals J, Shiyanovskii S, Wei QH, Lavrentovich OD. 2015 Liquid crystals with patterned molecular orientation as an electrolytic active medium. *Phys. Rev. E* **92**, 052502. (doi:10.1103/PhysRevE.92.052502)
80. Peng C, Turiv T, Guo Y, Wei QH, Lavrentovich OD. 2018 Sorting and separation of microparticles by surface properties using liquid crystal-enabled electro-osmosis. *Liq. Cryst.* **45**, 1936. (doi:10.1080/02678292.2018.1481539)
81. Baza H, Turiv T, Li BX, Li R, Yavitt BM, Fukuto M, Lavrentovich OD. 2020 Shear-induced polydomain structures of nematic lyotropic chromonic liquid crystal disodium cromoglycate. *Soft Matter* **16**, 8565. (doi:10.1039/D0SM01259A)
82. Zhang Q, Zhang R, Ge B, Yaqoob Z, So PTC, Bischofberger I. 2021 Structures and topological defects in pressure-driven lyotropic chromonic liquid crystals. *Proc. Natl Acad. Sci. USA* **118**, e2108361118. (doi:10.1073/pnas.2108361118)
83. Alama S, Bronsard L, Lamy X. 2016 Analytical description of the Saturn-ring defect in nematic colloids. *Phys. Rev. E* **93**, 012705. (doi:10.1103/PhysRevE.93.012705)
84. Genkin MM, Sokolov A, Lavrentovich OD, Aranson IS. 2017 Topological defects in a living nematic ensnare swimming bacteria. *Phys. Rev. X* **7**, 011029. (doi:10.1103/PhysRevX.7.011029)
85. Copenhagen K, Alert R, Wingreen NS, Shaevitz JW. 2021 Topological defects promote layer formation in *Myxococcus xanthus* colonies. *Nat. Phys.* **17**, 211–215. (doi:10.1038/s41567-020-01056-4)
86. Leslie FM. 1992 Continuum theory for nematic liquid crystals. *Continuum Mech. Thermodyn.* **4**, 167–175. (doi:10.1007/BF01130288)
87. Horn BLV, Winter HH. 2000 Dynamics of shear aligning of nematic liquid crystal monodomains. *Rheol. Acta* **39**, 294–300. (doi:10.1007/s003970000111)
88. Yeomans J. 2016 The hydrodynamics of active systems. (http://arxiv.org/abs/1603.00194v1 [cond-mat.soft]).
89. Emeršič T, Zhang R, Žiga K, Čopar S, Osterman N, de Pablo JJ, Tkalec U. 2019 Sculpting stable structures in pure liquids. *Sci. Adv.* **5**, eaav4283 (doi:10.1126/sciadv.aav4283)
90. Tang X, Selinger JV. 2020 Minimization principle for shear alignment of liquid crystals. *Phys. Rev. E* **101**, 032701 (doi:10.1103/PhysRevE.101.032701)
91. Murza AC, Teruel AE, Zarnescu AD. 2018 Shear flow dynamics in the Beris-Edwards model of nematic liquid crystals. *Proc. R. Soc. A* **471**, 20170673. (doi:10.1098/rspa.2017.0673)
92. Kleman M. 1989 Defects in liquid crystals. *Rep. Prog. Phys.* **52**, 555 (doi:10.1088/0034-4885/52/5/002)
93. Marchetti M, Joanny J, Ramaswamy S, Liverpool T, Prost J, Rao M, Simha RA. 2013 Hydrodynamics of soft active matter. *Rev. Mod. Phys.* **85**, 1143. (doi:10.1103/RevModPhys.85.1143)
94. Shankar S, Marchetti MC. 2019 Hydrodynamics of active defects: from order to chaos to defect ordering. *Phys. Rev. X* **9**, 041047. (doi:10.1103/PhysRevX.9.041047)
95. Kibble TWB. 1997 Phase transitions and topological defects in the early universe. *Aust. J. Phys.* **50**, 697. (doi:10.1071/P96076)
96. Schimming CD, Viñals J. 2023 Kinematics and dynamics of disclination lines in three-dimensional nematics. Figshare. (doi:10.6084/m9.figshare.c.6644164)